



# Hierarchical nanocomposite electrocatalyst of bimetallic zeolitic imidazolate framework and MoS<sub>2</sub> sheets for non-Pt methanol oxidation and water splitting

Yongkang Liu<sup>1</sup>, Bin Hu<sup>1</sup>, Shide Wu, Minghua Wang, Zhihong Zhang\*, Bingbing Cui, Linghao He\*, Miao Du\*

Henan Provincial Key Laboratory of Surface and Interface Science, Zhengzhou University of Light Industry, Zhengzhou 450002, China

## ARTICLE INFO

### Keywords:

Methanol oxidation reaction  
Hydrogen evolution reaction  
Oxygen evolution reaction  
CoNi-zeolitic imidazole framework  
MoS<sub>2</sub> nanosheets

## ABSTRACT

We have explored a nanocomposite composed of a bimetallic CoNi-zeolitic imidazole framework embedded by MoS<sub>2</sub> nanosheets (MoS<sub>2</sub>@CoNi-ZIF), as a bifunctional electrocatalyst for non-Pt methanol oxidation reaction (MOR) and overall water splitting in an alkaline solution. The series of MoS<sub>2</sub>@CoNi-ZIF nanocomposites exhibit different catalytic activities. Significantly, the MoS<sub>2</sub>@CoNi-ZIF nanosheet with a ratio of MoS<sub>2</sub>:CoNi-ZIF = 3:1 (MoS<sub>2</sub>@CoNi-ZIF(3-1)) shows the excellent electrocatalytic activity for MOR, affording an oxidation potential at 1.6 V, also with high catalytic current density and durability. Moreover, the MoS<sub>2</sub>@CoNi-ZIF(3-1) nanocomposite shows a superior electrocatalytic performance toward HER and OER. When the MoS<sub>2</sub>@CoNi-ZIF(3-1) was applied as the bifunctional catalyst for both the anode and cathode, the voltage applied to a two-electrode cell is 1.55 V to achieve a current density of 10 mA cm<sup>-2</sup> for overall water splitting. This work provides a promising electrocatalyst for developing high-performance non-Pt-based clean energy and fuel cells in alkaline solution.

## 1. Introduction

The demand for efficient energy conversion and storage systems has boosted considerable research efforts on developing novel electrocatalysts applied in the fields of advanced energy devices. A direct methanol fuel cell (DMFC) has employed to settle the present energy crisis by an environmentally friendly way. In DMFCs, methanol oxidation reaction (MOR) is a key step in the exploitation of fuel cell technology, where the precious metal platinum (Pt) exhibits the best catalytic activity [1]. However, the high cost, CO poisoning effect, and slow MOR kinetics are the main disadvantages of Pt-based electrocatalysts, thereby hampering their commercialization applications. As a result, researchers have recently devoted to develop alternative non-noble metal MOR electrocatalysts with highly activity and CO poisoning tolerance. Also, as one of the renewable energy sources, hydrogen (H<sub>2</sub>) can be achieved by electrochemical water splitting [2]. Nevertheless, the practical application of electrochemical water splitting for H<sub>2</sub> production is quite limited because the electrocatalytic efficiency of water splitting is depended on hydrogen evolution reaction (HER) and oxygen evolution reaction (OER). Among them, the OER is always limited by its

slow sluggish kinetics and the need of a large overpotential [3]. Normally, Pt and RuO<sub>2</sub> are mostly applied as the electrocatalysts for HER and OER, respectively. However, their scarce supply and high cost largely limit their practical exploitation. Furthermore, constructing bifunctional electrocatalysts for both OER and HER in a whole water-splitting cell is still challenging because of the mismatch of high concentrations of H<sup>+</sup> and OH<sup>-</sup> [4]. To overcome these issues, the development of non-precious-based catalysts with both excellent catalytic activity and high conductivity remains a great challenge. Transition metals and their derivatives are highly efficient alternatives in the field of clean and sustainable energy [3]. NiCo<sub>2</sub>O<sub>4</sub> [5], Ni<sub>0.75</sub>Cu<sub>0.25</sub> alloy [6], Mn doped Ni(OH)<sub>2</sub> [7] etc have been employed as anodic materials in MOR while transition metal chalcogenides, oxides/hydroxides, nitrides phosphides, and some metal-free materials have been used for overall water splitting [8]. However, their fabrication processes are usually very complicated, or additives are needed to deteriorate their performances.

Recent studies have shown that the active sites of electrocatalysts are often located in micro- and mesopores whereas the macro-pores are favorable to diffusion of species [9]. Therefore, porous materials are

\* Corresponding authors.

E-mail addresses: [2006025@zzuli.edu.cn](mailto:2006025@zzuli.edu.cn) (Z. Zhang), [helinghao@zzuli.edu.cn](mailto:helinghao@zzuli.edu.cn) (L. He), [dumiao@zzuli.edu.cn](mailto:dumiao@zzuli.edu.cn) (M. Du).

<sup>1</sup> These authors contributed equally.

considered to be ideal electrocatalyst candidates with high catalytic activity. Metal–organic frameworks (MOFs) have been regarded as ideal precursors or sacrificial templates to fabricate porous functional materials with promising applications in electrochemical aptasensors [10], Li-ion batteries [11], and photocatalysts and so on [12]. As a subclass of MOFs, zeolitic imidazole frameworks (ZIFs), have been emerged as suitable precursors for the development of structure-tailored nanocarbon frameworks due to their abundant pores, versatile surfaces, and high specific surface areas [13]. In particular, a Co-based ZIF, ZIF-67, with imidazolate as linkers has been used to synthesize various Co-containing electrocatalysts [14]. Moreover, Xiao et al. have fabricated cobalt-based bimetallic phosphide ultrathin nanosheets (CoM-P-NS, M = Ni, Mn, Cu, Zn) for highly efficient oxygen evolution in alkaline media [15]. Wen et al. have reported an MXene supported CoNi-ZIF-67 hybrid (CoNi-ZIF-67@Ti<sub>3</sub>C<sub>2</sub>T<sub>x</sub>) as an excellent OER electrocatalyst through in-situ growth of bimetallic CoNi-ZIF-67 rhombic dodecahedrons on the Ti<sub>3</sub>C<sub>2</sub>T<sub>x</sub> matrix [16]. Nevertheless, these materials only can be employed as a single catalyst, not bi- or tri-functional catalyst. In fact, there is no successful example for the use of ZIF as MOR catalyst. Besides, it is worthwhile to note that most bifunctional water splitting electrocatalysts have been synthesized by combining the doping of rare metal ions and calcining at high temperatures, further requiring costly electrocatalysts and tedious preparation procedures [17].

To improve the catalytic efficiency, a catalyst with large amounts of active sites and porous nanostructure for the fast transfer of electrons or ions can be developed by optimizing the morphology and composition [18]. Ultrathin two-dimensional (2D) nanosheets (NSs) exhibit excellent catalytic performances because of highly intrinsic activity and ultrahigh specific surface area [14]. Owing to homogeneous chemical composition and unique porous structure, a family of Co-based bimetallic phosphide NSs (CoM-P-NS, M = Ni, Mn, Cu and Zn) have been fabricated using ultrathin MOF NSs as precursors, giving abundant active sites, fast mass transport, and dynamic modulations toward OER [15]. A 2D-layered composite composed of metallic Co and N-carbon exhibits a low overpotential of 103 mV (vs. reversible hydrogen electrode (RHE)) at 10 mA cm<sup>-2</sup>, along with a high cycle durability and a considerable long-term stability for HER [19]. Nevertheless, pure 2D MOFs have been rarely used as electrocatalysts without post-treatment or calcination due to the inferior electrocatalytic activity. Therefore, effective strategies should be developed to fabricate ultrathin 2D MOF-based composite NSs, which can not only enlarge the 2D material family but also boost their practical applications in energy fields. However, only Co-MOF/graphene oxide composite [20], Cu-MOF [21], and electro-active pyridine-containing MOFs [22] have been explored to catalyze MOR. Thus, it is extremely interesting to develop multifunctional electrocatalysts for overall water splitting and MOR via a feasible approach. Additionally, MoS<sub>2</sub>, as a typical transition metal sulfide, is regarded as a promising catalyst, especially toward HER, because of its good chemical stability, low cost, and excellent electrocatalytic properties [23,24]. However, the electrocatalytic activity of MoS<sub>2</sub> may be limited by feasible aggregation and weak conductivity. Enhancing the electrical conductivity or synthesizing MoS<sub>2</sub> nanoarchitectures is highly urgent [25].

Based on above analysis, CoNi-ZIF and MoS<sub>2</sub> NSs may be combined to construct a novel multifunctional catalyst without further treatment. In this work, we have proposed a series of hierarchical nanostructured composites of bimetallic CoNi-ZIF and MoS<sub>2</sub> NSs (MoS<sub>2</sub>@CoNi-ZIF) and first explored them as the trifunctional electrocatalysts for MOR, HER, and OER in an alkaline solution (Scheme 1). The electrocatalytic activity of MoS<sub>2</sub>@CoNi-ZIF composite with a MoS<sub>2</sub>:CoNi-ZIF ratio of 3:1 (MoS<sub>2</sub>@CoNi-ZIF(3-1)) outperforms others, including MoS<sub>2</sub>, CoNi-ZIF, MoS<sub>2</sub>@CoNi-ZIF(1-1), and MoS<sub>2</sub>@CoNi-ZIF(5-1). The proposed MoS<sub>2</sub>@CoNi-ZIF(3-1) catalyst shows three advantages, namely, (i) multiple catalytic performances for MOR with an oxidation potential of 1.6 V and for water splitting with a low potential of 1.55 V to achieve a

stable current density of 10 mA cm<sup>-2</sup> in an alkaline solution, (ii) synthesis without requiring calcination or other treatments, and (iii) strong synergistic effect among CoNi-ZIF, metal oxide, and MoS<sub>2</sub>, providing the MoS<sub>2</sub>@CoNi-ZIF catalyst with a comprehensive performance and high stability in aqueous solution.

## 2. Experimental section

### 2.1. Reagents and materials

Cobaltous nitrate (Co(NO<sub>3</sub>)<sub>2</sub>·6H<sub>2</sub>O), nickelous nitrate (Ni(NO<sub>3</sub>)<sub>2</sub>·6H<sub>2</sub>O), and 2-methylimidazole (C<sub>4</sub>H<sub>6</sub>N<sub>2</sub>) were purchased from Aladdin Chemical Reagent Co. Ltd. (Shanghai, China). Sodium molybdate (Na<sub>2</sub>MoO<sub>4</sub>·2H<sub>2</sub>O), thioacetamide (CH<sub>3</sub>CSNH<sub>2</sub>), potassium hydroxide (KOH), ethanol (C<sub>2</sub>H<sub>5</sub>OH), and methanol (CH<sub>3</sub>OH) were purchased from Sinopharm Chemical Reagent Co., Ltd. (Shanghai, China). All reagents were of analytical grade and used without further purification.

### 2.2. Synthesis of MoS<sub>2</sub> NSs

MoS<sub>2</sub> NSs were prepared according to the literature [26]. In brief, 50 mg Na<sub>2</sub>MoO<sub>4</sub>·2H<sub>2</sub>O was dissolved in 20 mL of Milli-Q water, while 50 mg CH<sub>3</sub>CSNH<sub>2</sub> was dissolved in 20 mL of ethanol. Subsequently, the CH<sub>3</sub>CSNH<sub>2</sub> solution was slowly added into the Na<sub>2</sub>MoO<sub>4</sub>·2H<sub>2</sub>O solution, followed by sonication for 30 min. Afterward, the mixture was transferred to the Teflon-lined stainless-steel autoclave (50 mL) and heated at 200 °C for 12 h. The product was rinsed with ethanol and then dried at 60 °C for 12 h.

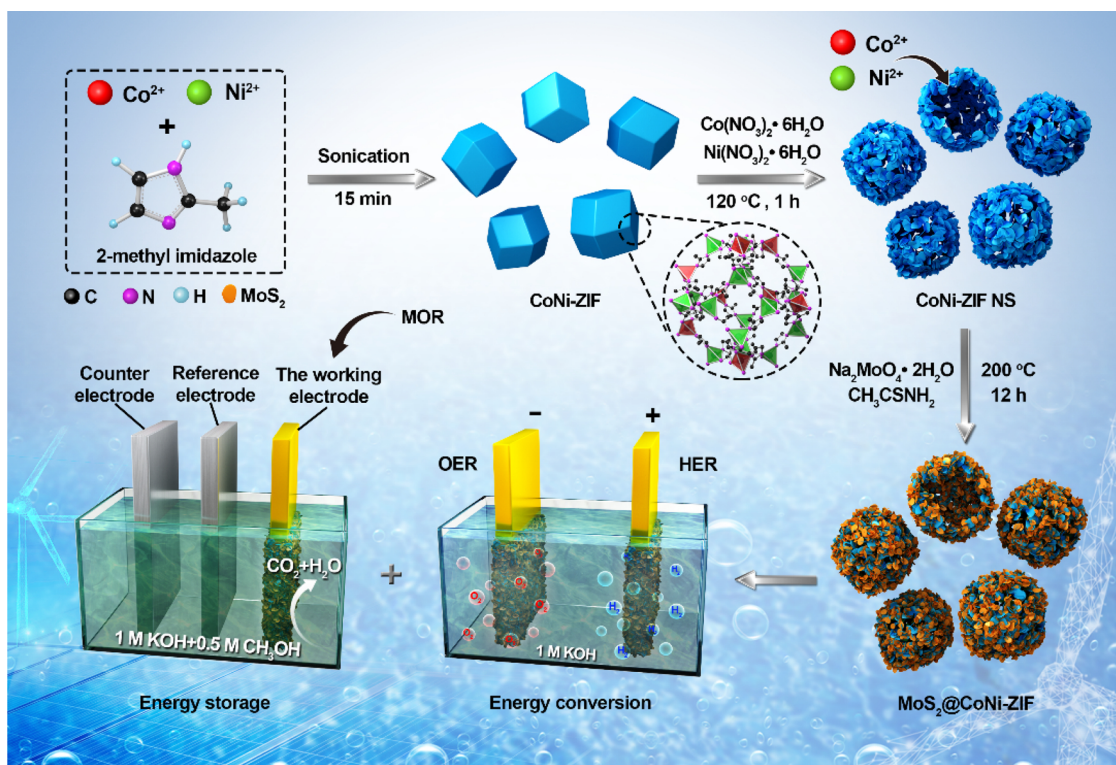
### 2.3. Preparation of CoNi-ZIF NSs and MoS<sub>2</sub>@CoNi-ZIF composites

The CoNi-ZIF NSs were synthesized by a modified method according to literature [15]. Briefly, 0.55 g Co(NO<sub>3</sub>)<sub>2</sub>·6H<sub>2</sub>O and 0.55 g Ni(NO<sub>3</sub>)<sub>2</sub>·6H<sub>2</sub>O were dissolved in methanol (30 mL) under magnetic stirring to form the solution I. Two copies of the solution I were prepared for further use. 1.32 g 2-methylimidazole was dissolved in methanol (30 mL) under magnetic stirring to afford the solution II. Then, the solution I was added into the solution II, followed by sonication for 15 min. The mixture was washed by methanol, dispersed in methanol (30 mL) and mixed with the solution I. Then, the mixture was moved into a Teflon-lined stainless-steel autoclave (100 mL) and heated at 120 °C for 1 h. Finally, the CoNi-ZIF NSs were rinsed with ethanol and dried at 60 °C for overnight.

For the preparation of the series of MoS<sub>2</sub>@CoNi-ZIF composites, the as-synthesized MoS<sub>2</sub> NSs with different dosages were added in the synthetic system of CoNi-ZIF NSs. According to the ratios of MoS<sub>2</sub>:CoNi-ZIF NSs (i.e., 1:1, 3:1, and 5:1), the composites were represented by MoS<sub>2</sub>@CoNi-ZIF(1-1), MoS<sub>2</sub>@CoNi-ZIF(3-1), and MoS<sub>2</sub>@CoNi-ZIF(5-1), respectively.

### 2.4. Physicochemical characterizations

X-ray diffraction (XRD) measurement was performed on a Rigaku D/Max-2500 X-ray diffractometer using Cu K<sub>α</sub> radiation with the scanning 2θ angle of 5–70°. X-ray photoelectron spectroscopy (XPS) data were measured on a Thermo Fisher ESCALAB 250Xi photoelectron spectrometer equipped with an Al anode (Al-K<sub>α</sub> 1486.6 eV). The surface morphologies of all samples were investigated on a JSM-6490LV field emission scanning electron microscope (FE-SEM, Japan) and JEOL JEM-2100 transmission electron microscopy (TEM) with a field emission gun of 200 kV. N<sub>2</sub> adsorption and desorption isotherms were collected on a Micromeritics 3Flex surface area and pore size analyzer under ultrahigh vacuum in a clean system.



**Scheme 1.** Schematic diagram of the preparation of  $\text{MoS}_2@\text{CoNi-ZIF}$  catalysts and electrocatalytic performances for MOR and overall water splitting.

## 2.5. Electrochemical measurements

The catalyst (1.0 mg) was dispersed into 1.0 mL of Milli-Q water to form a homogeneous ink under sonication. Then, 10  $\mu\text{L}$  of the ink was dropped onto the rotating-disk-electrode (RDE) surface (3.0 mm diameter) by a transfer liquid gun and dried naturally. Accordingly, the mass loading of active materials is  $0.143 \text{ mg cm}^{-2}$ . All electrochemical measurements were taken on a CHI 760E electrochemical workstation equipped with a conventional three-electrode cell with 1.0 M KOH as the electrolyte solution, of which a Pt wire, silver/silver chloride (Ag/AgCl) electrode, and RDE covered with a thin catalyst film were employed as the counter, reference, and working electrodes, respectively. Methanol oxidation measurements were carried out using cyclic voltammetry (CV) with the scan rate of  $50 \text{ mV s}^{-1}$ , using 0.5 M  $\text{CH}_3\text{OH}$  in 1.0 M KOH electrolyte. Electrochemical double-layer capacitance measurements of the working electrode were performed by using CV curves for two cycles between 1.12 and 1.22 V vs. RHE with scanning rates of 10, 20, 30, 40, 50, 60, 70, 80, 90, and  $100 \text{ mV s}^{-1}$ . The current density differences between the minimum and maximum values at 1.17 V vs. RHE and the corresponding scanning rates were used to calculate the EDLC values. All potentials were  $iR$  corrected and referenced to RHE by the equation:  $E_{\text{RHE}} = E_{\text{Ag/AgCl}} + (0.197 + 0.0591 \times \text{pH}) \text{ V}$ .

The OER or HER activities and overall water splitting were characterized by linear sweep voltammetry (LSV) with the scan rate of  $10 \text{ mV s}^{-1}$ . RDE and glass carbon electrode (GCE) of 3 mm in diameter were used as the working electrode in OER and HER tests, respectively. In the two-electrode configuration of overall water splitting,  $\text{MoS}_2@\text{CoNi-ZIF}$  catalysts were used as both cathode and anode for HER and OER, respectively. Electrochemical impedance spectroscopy (EIS) measurements were taken in the potentiostatic state from 0.01 to  $10^5 \text{ Hz}$  with a modulation amplitude of 10 mV. Chronopotentiometry tests were implemented at a current density of  $10 \text{ mA cm}^{-2}$ . Overall water splitting was performed in a two-electrode system where the positive electrode and negative electrode used the same materials.

## 3. Results and discussion

### 3.1. Crystal and chemical structures of the series of $\text{MoS}_2@\text{CoNi-ZIF}$ NSs

The crystal structures of the series of  $\text{MoS}_2@\text{CoNi-ZIF}$  NSs were characterized by XRD (Fig. 1a). The XRD pattern of  $\text{MoS}_2$  demonstrates (curve i) four clear diffraction peaks, which are due to the hexagonal structure of  $\text{MoS}_2$  (JCPDS card no. 77-1716). Additionally, the concomitant appearance of four distinctive diffraction peaks can be detected at  $10.2^\circ$ ,  $20.1^\circ$ ,  $34.0^\circ$ , and  $60.2^\circ$  for CoNi-ZIF NSs (curve ii) [15]. After  $\text{MoS}_2$  NSs were coated onto surface of CoNi-ZIF, the diffraction peaks for  $\text{MoS}_2@\text{CoNi-ZIF}(1-1)$ ,  $\text{MoS}_2@\text{CoNi-ZIF}(3-1)$  (curve iv), and  $\text{MoS}_2@\text{CoNi-ZIF}(5-1)$  (curve v) are different, in which the peak located at  $9.2^\circ$  is attributed to  $\text{MoS}_2$ . Nevertheless, no CoNi-ZIF characterized peak is observed, which is mainly due to the full coverage of the thick  $\text{MoS}_2$  NSs over CoNi-ZIF NSs. Even the peaks at  $38.4^\circ$  and  $55.2^\circ$  of  $\text{MoS}_2$  are not observed in CoNi-ZIF@ $\text{MoS}_2(1-1)$  composite, they appear in  $\text{MoS}_2@\text{CoNi-ZIF}(3-1)$  and  $\text{MoS}_2@\text{CoNi-ZIF}(5-1)$  composites as the amount of  $\text{MoS}_2$  increases.

The Raman spectra of all samples were taken to evaluate their chemical structures (Fig. 1b).  $\text{MoS}_2$  NSs illustrate two main peaks at  $376$  and  $406 \text{ cm}^{-1}$ , corresponding to the  $E_{2g}^1$  and  $A_{1g}$  modes of the hexagonal  $\text{MoS}_2$  crystal, respectively [27]. The peak located at  $1576 \text{ cm}^{-1}$  is assigned to the G-band, which is often referred to the “disorder” band, while the peak at  $1357 \text{ cm}^{-1}$  is assigned to the D-band presented in the  $sp^2$  hybridized carbon materials and derived from the  $E_{2g}$  vibrational mode [28]. For the CoNi-ZIF NSs, the bands centered at  $473$  and  $516 \text{ cm}^{-1}$  are assigned to Ni–O vibrations in CoNi-ZIF NSs [29]. The weak band at  $1046 \text{ cm}^{-1}$  is ascribed to the deformation mode of hydroxyl [30]. For  $\text{MoS}_2@\text{CoNi-ZIF}(1-1)$  (curve iii),  $\text{MoS}_2@\text{CoNi-ZIF}(3-1)$  (curve iv), and  $\text{MoS}_2@\text{CoNi-ZIF}(5-1)$  (curve v) NSs, the bands are assigned to  $\text{MoS}_2$  and CoNi-ZIF NSs, indicating the successful combination of  $\text{MoS}_2$  and CoNi-ZIF NSs.

Variations in chemical structures and components before and after combination of CoNi-ZIF and  $\text{MoS}_2$  with different dosages were evaluated by XPS (Fig. S1). The related discussion about the XPS results of



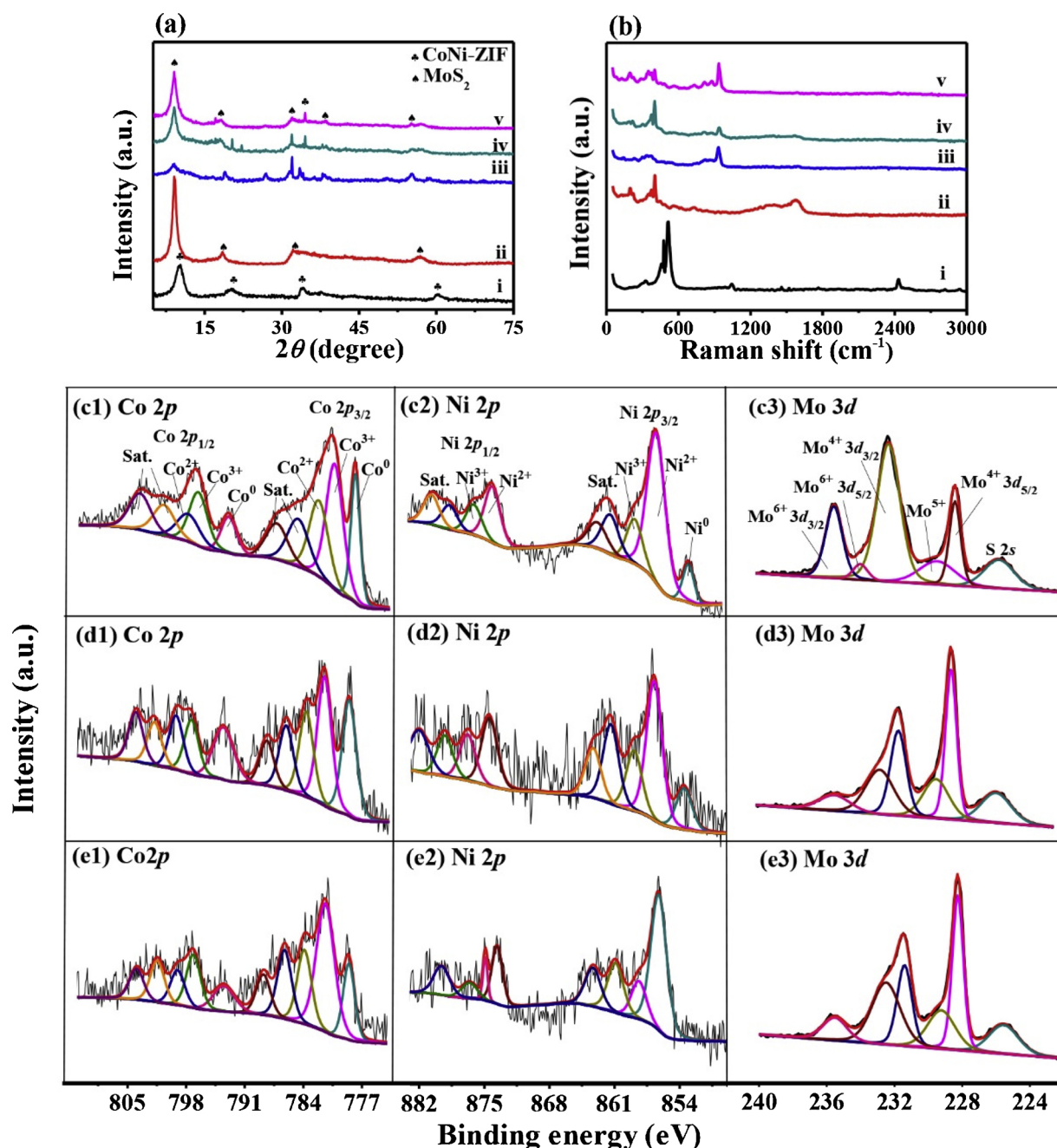


**Fig. 1.** (a) XRD and (b) Raman spectra of (i) CoNi-ZIF, (ii) MoS<sub>2</sub>, (iii) MoS<sub>2</sub>@CoNi-ZIF(1-1), (iv) MoS<sub>2</sub>@CoNi-ZIF(3-1) and (v) MoS<sub>2</sub>@CoNi-ZIF(5-1) NSs. Co 2p, Ni 2p, and Mo 2p core-level XPS spectra of (c) MoS<sub>2</sub>@CoNi-ZIF(1-1), (d) MoS<sub>2</sub>@CoNi-ZIF(3-1) and (e) MoS<sub>2</sub>@CoNi-ZIF(5-1) NSs.

pristine CoNi-ZIF and MoS<sub>2</sub> NSs are given in the part of S1 (Supplementary material). The high-resolution XPS spectra of each element containing in the series of MoS<sub>2</sub>@CoNi-ZIF NSs are summarized in Figs. 1c–e and S4. In the high-resolution Co 2p XPS spectra, apart from the characteristic peaks of Co<sup>2+</sup> and Co<sup>3+</sup> ions, two peaks at 778.2 and 793.2 eV of the metallic state of Co (Co<sup>0</sup>) is observed in all MoS<sub>2</sub>@CoNi-ZIF NSs [31]. This indicates that some Co<sup>2+</sup> ions were reduced to Co<sup>0</sup> during the preparation. Similarly, in addition to Ni<sup>2+</sup> and Ni<sup>3+</sup>, the metallic state of Ni (Ni<sup>0</sup>) is found at 852.7 eV in the high-resolution XPS spectrum of each sample [32]. The results reveal that Co<sup>2+</sup> or Ni<sup>2+</sup> species containing in CoNi-ZIF NSs will be partially reduced to their metallic states when thioacetamide was used. The coexistence of metallic Co and Ni contributes to the improvement of electrochemical activity [33]. The ratios of Co<sup>2+</sup>/Co<sup>3+</sup> and Ni<sup>2+</sup>/Ni<sup>3+</sup> and the contents of metallic Co and Ni were deduced based on the

relative intensity of each peak (Table S2). It demonstrates that the percentage of metallic states Co and Ni in MoS<sub>2</sub>@CoNi-ZIF(3-1) is highest. XPS data further suggest that the prepared MoS<sub>2</sub>@CoNi-ZIF composites are composed of Co<sup>3+</sup> and Ni<sup>2+</sup>, which can provide enough active sites for electrocatalysis [34]. The analysis of the high-resolution Mo 3d XPS spectra of the series of MoS<sub>2</sub>@CoNi-ZIF composites (Fig. 1c3, d3, and e3) reveals a similar result to that of pure MoS<sub>2</sub> (Fig. S2a), indicating its chemical stability. Abundant Mo<sup>4+</sup> species in MoS<sub>2</sub>@CoNi-ZIF composites facilitate the improvement of their electrocatalytic activity [35].

### 3.2. Surface morphologies of MoS<sub>2</sub>@CoNi-ZIF NSs

FE-SEM and TEM were used to explore the surface morphologies of the as-prepared MoS<sub>2</sub>, CoNi-ZIF, and series of MoS<sub>2</sub>@CoNi-ZIF



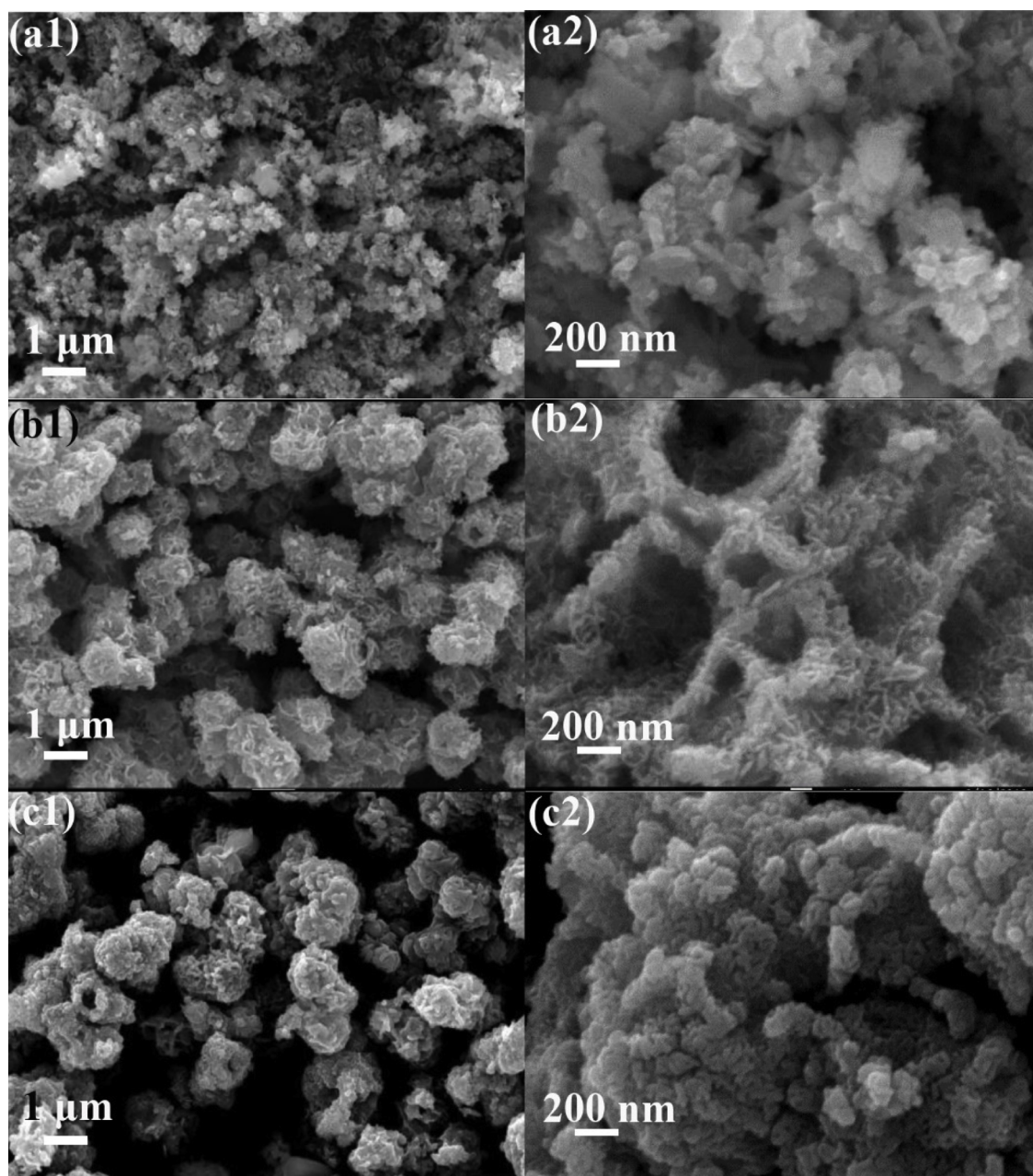


Fig. 2. Low- and high-magnification SEM images of (a1, a2)  $\text{MoS}_2$ @CoNi-ZIF(1-1), (b1, b2)  $\text{MoS}_2$ @CoNi-ZIF(3-1), and (c1, c2)  $\text{MoS}_2$ @CoNi-ZIF(5-1) NSs.

composites. The  $\text{MoS}_2$  NSs are aggregated into nanoparticles, while the ultrathin CoNi-ZIF NSs are assembled into hollow nanospheres (S2 in Supplementary material). It seems that the morphology of  $\text{MoS}_2$ @CoNi-ZIF changes as the amount of  $\text{MoS}_2$  increases (Fig. 2).  $\text{MoS}_2$ @CoNi-ZIF(1-1) composite is composed of NSs with various sizes, thereby accumulating into large blocks (Fig. 2a1 and a2).  $\text{MoS}_2$ @CoNi-ZIF(3-1) nanocomposite presents a flower-like nanostructure (Fig. 2b1 and b2), while CoNi-ZIF NSs become thick due to the growth of  $\text{MoS}_2$  on CoNi-ZIF surface. The original shape of CoNi-ZIF is not maintained in  $\text{MoS}_2$ @CoNi-ZIF(5-1) composite because the thick  $\text{MoS}_2$  layer negatively affects the crystallization behavior of CoNi-ZIF (Fig. 2c1 and c2).

In Fig. 3a1, the TEM image of  $\text{MoS}_2$ @CoNi-ZIF(1-1) composite shows that  $\text{MoS}_2$  NSs grow on surface of CoNi-ZIF, which is further confirmed by high-resolution TEM (HR-TEM) (Fig. 3a2 and a3). The crystal lattice fringe spacing ascribed to the  $\text{MoS}_2$  plane is present, whereas the lattice fringe spacings of 0.15 and 0.22 nm are attributed to (220) and (200) planes of CoO (Fig. 3a3), respectively [36]. In

$\text{MoS}_2$ @CoNi-ZIF(3-1) composite, the well distributed hollow nanospheres with 400 nm diameter are obtained, which are embedded by  $\text{MoS}_2$  NSs. In Fig. 3b3, the lattice fringe spacings of 0.22 and 0.24 nm in HR-TEM image indicate the (200) plane of CoO and (111) plane of NiO, respectively. This observation demonstrates that the  $\text{MoS}_2$  layer thickens around  $\text{MoS}_2$ @CoNi-ZIF(3-1), in which the lattice fringe spacing of CoO or NiO is not easily formed (Fig. 3c2 and c3). The EDS mapping analysis for  $\text{MoS}_2$ @CoNi-ZIF composites proves the homogeneous distribution of Co, Ni, and Mo (Fig. 4).

The  $\text{N}_2$  adsorption-desorption isotherms of  $\text{MoS}_2$ @CoNi-ZIF composites were explored (Fig. S7a). The CoNi-ZIF,  $\text{MoS}_2$ @CoNi-ZIF(1-1) and  $\text{MoS}_2$ @CoNi-ZIF(3-1) exhibit type IV adsorption curves with distinct hysteresis loops in the  $P/P_0$  range of 0.5–1.0, hinting their mesoporous nature that can also be confirmed by the pore size distribution [37]. As shown in Fig. S7b, CoNi-ZIF shows micro/mesoporous characteristic, while  $\text{MoS}_2$ @CoNi-ZIF composites show mesoporous feature. The specific surface area of CoNi-ZIF is estimated to be  $95.7 \text{ m}^2 \text{ g}^{-1}$ ,



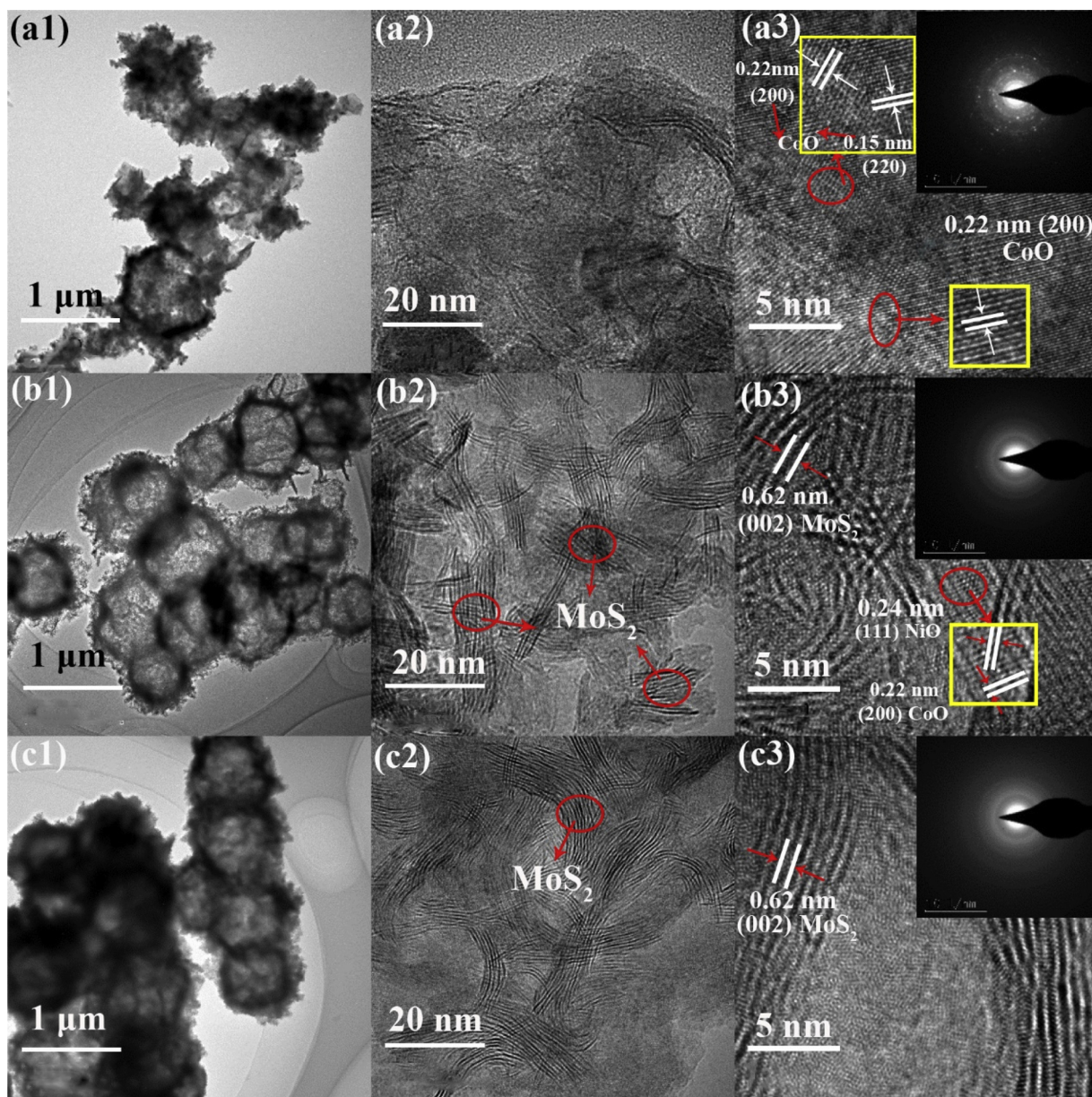


**Fig. 3.** TEM and HR-TEM images of (a1, a2, a3)  $\text{MoS}_2$ @CoNi-ZIF(1-1), (b1, b2, b3)  $\text{MoS}_2$ @CoNi-ZIF(3-1), and (c1, c2, c3)  $\text{MoS}_2$ @CoNi-ZIF(5-1) NSs (the insets of a3, b3, and c3: their corresponding SAED patterns).

whereas that of  $\text{MoS}_2$  NSs is only  $7.83 \text{ m}^2 \text{ g}^{-1}$ . As such, the combination of CoNi-ZIF and  $\text{MoS}_2$  results in the decrease of specific surface areas for  $\text{MoS}_2$ @CoNi-ZIF composites, which are evaluated to be 46.1, 33.8, and  $9.6 \text{ m}^2 \text{ g}^{-1}$ , for  $\text{MoS}_2$ @CoNi-ZIF(1-1),  $\text{MoS}_2$ @CoNi-ZIF(3-1), and  $\text{MoS}_2$ @CoNi-ZIF(5-1), respectively. The mesoporous void is helpful for the efficient mass transport in the electrocatalytic reaction, but this is not the sole factor that affects the catalytic activity [38].

### 3.3. Electrochemical MOR performances of $\text{MoS}_2$ @CoNi-ZIF in the alkaline solution

Considering the excellent MOR performances of both  $\text{MoS}_2$ - and CoNi-related materials, MOR properties of the series of  $\text{MoS}_2$ @CoNi-ZIF composites were studied. The CV curves of  $\text{MoS}_2$ , CoNi-ZIF, and  $\text{MoS}_2$ @CoNi-ZIF composites were measured in 1.0 M KOH solution at the scan rate of  $50 \text{ mV s}^{-1}$  (Fig. 5a). No obvious redox peak is found in CV curve of  $\text{MoS}_2$ -modified electrode, suggesting its poor electrochemical activity. For  $\text{MoS}_2$ @CoNi-ZIF composites, the CV curves are

nonrectangular, indicating the reversible redox reactions. Notably, the  $\text{MoS}_2$ @CoNi-ZIF(3-1)-modified electrode shows a pair of well-defined redox peaks consisting of an anodic peak at 0.42 V and a cathodic peak at 0.26 V. These peaks are attributed to the oxidation of  $\text{Co}^{2+}$  and reduction of  $\text{Ni}^{3+}$ . Previous research reveals that  $\text{Co}^0$ ,  $\text{Co}^{2+}$ , and  $\text{Co}^{3+}$  can undergo electrochemical charge transfer reactions of  $\text{Co}^0 \leftrightarrow \text{Co}^{2+} \leftrightarrow \text{Co}^{3+} \leftrightarrow \text{Co}^{4+}$  in alkaline solutions [39]. The redox process of  $\text{Ni}^0/\text{Ni}^{2+}/\text{Ni}^{3+}$  can also occur [40]. In this case, the peaks caused by each redox couple are not distinct, and only one pair of redox peaks situated at 0.26 V/0.42 V (vs. RHE) is clearly observed. This may be because the electrochemical reactions of  $\text{Co}^{2+}/\text{Co}^{3+}$  and  $\text{Ni}^{2+}/\text{Ni}^{3+}$  simultaneously occur, resulting in the overlap of redox peaks. Among the CV curves of the three  $\text{MoS}_2$ @CoNi-ZIF composites, the  $\text{MoS}_2$ @CoNi-ZIF(3-1)-modified electrode shows the highest peak current density and the largest enclosed area, indicating that the redox current density of this electrode is superior to that of other  $\text{MoS}_2$ @CoNi-ZIF-based electrodes. The contents of the metallic state Co/Ni and the ratios of  $\text{Co}^{2+}/\text{Co}^{3+}$  and  $\text{Ni}^{3+}/\text{Ni}^{2+}$  in the  $\text{MoS}_2$ @CoNi-ZIF(3-1) catalyst are the highest,



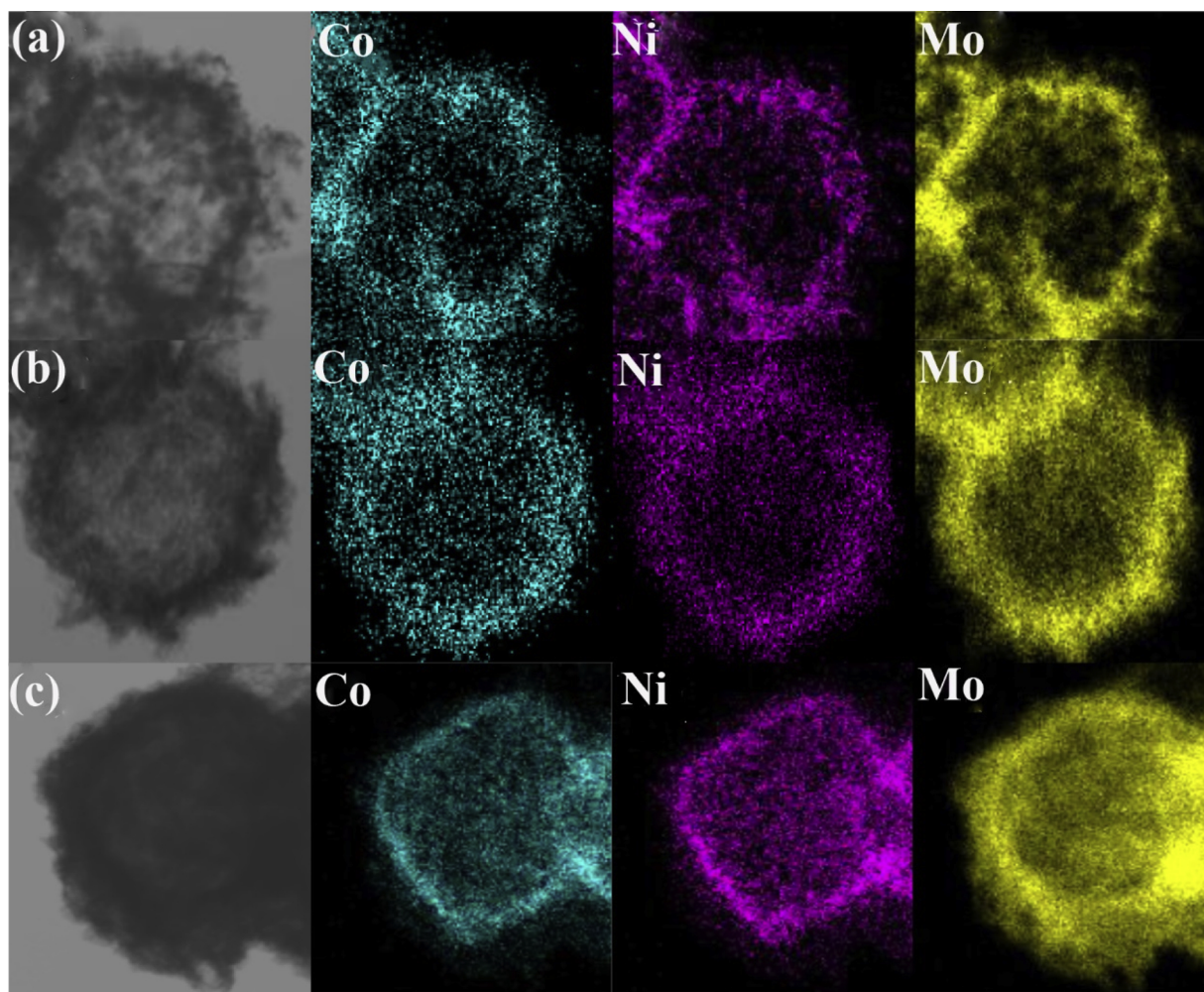


**Fig. 4.** Elemental mapping of homogeneously distributed Co (cyan), Ni (purple), and Mo (yellow) containing in the series of (a)  $\text{MoS}_2$ @CoNi-ZIF(1-1), (b)  $\text{MoS}_2$ @CoNi-ZIF(3-1), and (c)  $\text{MoS}_2$ @CoNi-ZIF(5-1) NSs. (For interpretation of the references to colour in this figure legend, the reader is referred to the web version of this article.)

suggesting the superior electrocatalytic activity of this catalyst.

The MOR activities of  $\text{MoS}_2$ , CoNi-ZIF and  $\text{MoS}_2$ @CoNi-ZIF composites were examined by adding the mixed solution of 1.0 M KOH and 0.5 M  $\text{CH}_3\text{OH}$  (Fig. 4b). The results show the electro-oxidation reactions of  $\text{CH}_3\text{OH}$  on the electrodes modified by these materials except for  $\text{MoS}_2$ . The anodic currents of methanol oxidation for all  $\text{MoS}_2$ @CoNi-ZIF catalysts sharply increase. The maximum current densities of methanol oxidation for  $\text{MoS}_2$ , CoNi-ZIF,  $\text{MoS}_2$ @CoNi-ZIF(1-1),  $\text{MoS}_2$ @CoNi-ZIF(3-1), and  $\text{MoS}_2$ @CoNi-ZIF(5-1) catalysts at 0.6 V are 27.65, 86.24, 191.38, 430.08, and 229.32  $\text{mA g}^{-1}$ , respectively. In addition, onset potential is a critical parameter for evaluating the MOR catalytic performance. Fig. 5b shows that the onset potentials of  $\text{MoS}_2$ , CoNi-ZIF,  $\text{MoS}_2$ @CoNi-ZIF(1-1),  $\text{MoS}_2$ @CoNi-ZIF(3-1), and  $\text{MoS}_2$ @CoNi-ZIF(5-1) are 1.43, 1.31, 1.26, 1.24, and 1.3 V, respectively. That is to say, the catalytic activity of  $\text{MoS}_2$ @CoNi-ZIF(3-1)-based electrode outperforms the electrodes based on other materials. The obtained onset potential of  $\text{MoS}_2$ @CoNi-ZIF(3-1)-based electrode is smaller than that reported in previous studies of metal oxide-based electrocatalysts for MOR [41]. Fig. S8 illustrates that the CV curve of  $\text{MoS}_2$ @CoNi-ZIF(3-1) measured in 1.0 M KOH is quite different from that measured in the mixed solution of KOH and  $\text{CH}_3\text{OH}$ . The onset potential of  $\text{MoS}_2$ @CoNi-ZIF(3-1) catalyst of MOR is around 0.1 V, and even the individual CoNi-ZIF and  $\text{MoS}_2$  catalysts exhibit poor electrochemical activity. Their integration can enhance the electro-oxidation ability, indicating that the as-prepared  $\text{MoS}_2$ @CoNi-ZIF(3-1)-modified

electrode can be used as an efficient MOR catalyst in alkaline solution. Herein, all potentials were converted to the ones of RHE for an equal comparison, and the synergistic electrocatalytic activity of the  $\text{MoS}_2$ @CoNi-ZIF(3-1) electrode in MOR was assessed by comparing the mass activities with other catalysts (Fig. 5b inset). The mass activity of  $\text{MoS}_2$ @CoNi-ZIF(3-1) is 430.08  $\text{mA g}^{-1}$ , which is 2.25, 1.88, 4.99, and 15.56 times higher than those of  $\text{MoS}_2$ @CoNi-ZIF(1-1) (191.38  $\text{mA g}^{-1}$ ),  $\text{MoS}_2$ @CoNi-ZIF(5-1) (229.32  $\text{mA g}^{-1}$ ), CoNi-ZIF (86.24  $\text{mA g}^{-1}$ ), and  $\text{MoS}_2$  (27.65  $\text{mA g}^{-1}$ ), respectively.

In Fig. 5c, the CVs recorded in  $\text{CH}_3\text{OH}$  solution with different concentrations from 0.2 to 0.7 M reveal the influence of  $\text{CH}_3\text{OH}$  concentration on MOR electrocatalytic activity of the  $\text{MoS}_2$ @CoNi-ZIF(3-1)-modified electrode, showing that the anodic peak current increases with the increase of  $\text{CH}_3\text{OH}$  concentration. This reveals a typical electrocatalytic response of MOR. Additionally, the maximum current density is proportional to  $\text{CH}_3\text{OH}$  concentration (Fig. 5c inset). The CV curve was also measured on the  $\text{MoS}_2$ @CoNi-ZIF(3-1)-modified electrode with the scan rate increasing from 20 to 300  $\text{mV s}^{-1}$ , but no obvious change in the shape of CV curves is found due to the fast reaction kinetics, which originates from the porous structure and fast electron transfer of electroactive materials [42]. The linear relationship obtained from the methanol oxidation peak current and the square root of scan rate reveals a diffusion-controlled process of the electrocatalytic reaction [43]. Oxidation potential and methanol oxidation current are essential parameters for performance assessment of MOR catalysts.



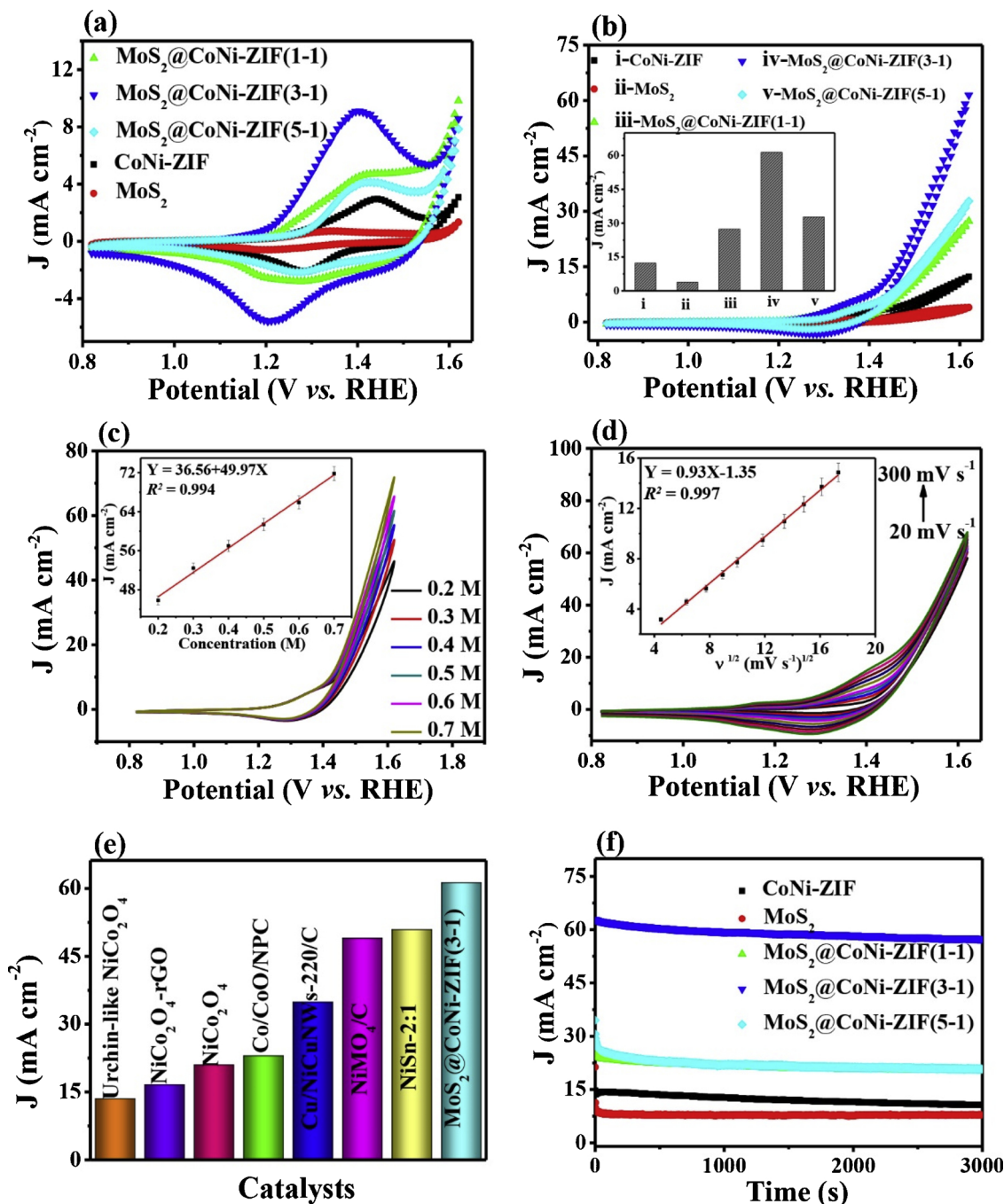


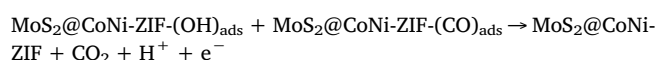
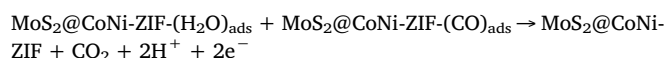
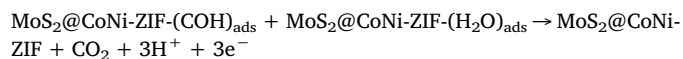
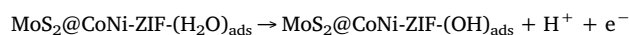
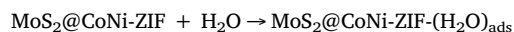
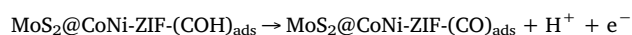
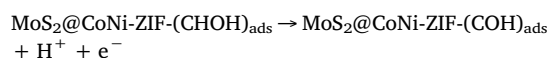
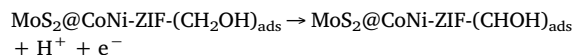
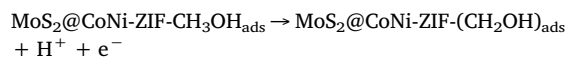
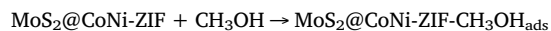
**Fig. 5.** (a) CVs of CoNi-ZIF, MoS<sub>2</sub>, MoS<sub>2</sub>@CoNi-ZIF(1-1), MoS<sub>2</sub>@CoNi-ZIF(3-1), and MoS<sub>2</sub>@CoNi-ZIF(5-1) recorded in 1.0 M KOH solution and (b) 1.0 M KOH + 0.5 M CH<sub>3</sub>OH at the scan rate of 50 mV s<sup>-1</sup>. (c) CV curves of MoS<sub>2</sub>@CoNi-ZIF(3-1) in the CH<sub>3</sub>OH solution with different concentrations (inset: the relationship between the peak oxidation current at 1.6 V and concentration of CH<sub>3</sub>OH for MoS<sub>2</sub>@CoNi-ZIF(3-1)). (d) CV curves of MoS<sub>2</sub>@CoNi-ZIF(3-1) electrode in 1.0 M KOH solution at different scan rates (inset: the relationship of the anodic peak currents vs scan rates of MoS<sub>2</sub>@CoNi-ZIF(3-1) electrode). (e) Comparison of the reported catalysts of the current density. (f) Chronoamperometric curves of MoS<sub>2</sub>@CoNi-ZIF(3-1) recorded in 1.0 M KOH + 0.5 M CH<sub>3</sub>OH solution at 1.6 V potential before and after 3000 cycles between 0.8 and 1.6 V vs. RHE.

Compared with other state-of-the-art Co- or Ni-based catalysts (Table S3 and Fig. 5e), MoS<sub>2</sub>@CoNi-ZIF(3-1) exhibits a superior electrocatalytic activity, as confirmed by both high peak current density and low peak potential. Fig. 5f shows the chronoamperograms recorded for 3000 s in mixed solution of 1.0 M KOH and 0.5 M CH<sub>3</sub>OH. The potential was held at the oxidation peak potential during measurements. The current density sharply decreases at the beginning and then slightly decreases for poisoning of catalysts. Among them, the degradation rate of MoS<sub>2</sub>@CoNi-ZIF(3-1) is obviously less than those of other catalysts, revealing its excellent durability. Regarding to the dual pathway

mechanism of methanol oxidation, the intermediate species generated in the indirect pathway can be strongly immobilized on the catalyst surface to occupy the reaction active sites. It further results in a serious decrease in reaction kinetics and is responsible for the poisoning of catalytic sites [44]. The CV curve of MoS<sub>2</sub>@CoNi-ZIF(3-1) in MOR remains stable after 3000 cycles (Fig. S8b), indicating its good stability.

The Nyquist plots of all materials were investigated to explore the catalytic mechanism of MoS<sub>2</sub>@CoNi-ZIF(3-1) in MOR (Fig. S9), and the experimental data were simulated by an equivalent circuit model (Fig. S9 inset). The simulated equivalent circuit consists of charge transfer

resistance ( $R_{ct}$ ), solution resistance ( $R_s$ ), constant-phase element (CPE), and Warburg impedance ( $W_o$ ). A small  $R_{ct}$  value indicates the quick electron transfer on electrode surface [45]. Therefore, the smallest  $R_{ct}$  value of the  $\text{MoS}_2/\text{CoNi-ZIF}(3-1)$  electrode ( $32\ \Omega$ ) expresses the greatest electro-catalytic kinetics behavior of electro-oxidation. Accordingly to the basic characterizations and electrochemical behaviors, the electrocatalytic activity and stability of  $\text{MoS}_2/\text{CoNi-ZIF}$  could be attributed to the following factors: (i) a low onset potential and a quick electrode kinetics are the inherent factors that notably enhance the MOR activity; (ii) the architecture with functional mesopores, epitaxial  $\text{MoS}_2$  orientation and hierarchical voids facilitate the electron diffusion to active centers [46]; (iii) rich  $\text{Ni}^{2+}$ ,  $\text{Co}^{3+}$ , and  $\text{Mo}^{4+}$  active sites can efficiently strengthen the reaction kinetics, resulting in a remarkable electrocatalytic MOR performance [47,48]; and (iv) the synergistic effect of CoNi-ZIF and  $\text{MoS}_2$  leads to the MOR activity enhancement of the catalyst. In general, the combined effect of these factors will greatly improve both catalytic activity and stability of  $\text{MoS}_2/\text{CoNi-ZIF}$  catalyst. Additionally, the overall process of MOR undergoes some necessary elementary steps, such as adsorption of methanol, dehydrogenation of methanol into intermediates, and oxidation of these intermediates into  $\text{CO}_2$  [49]. When the MOR takes places, methanol is adsorbed on the  $\text{MoS}_2/\text{CoNi-ZIF}$  surface as well as CoNi-ZIF and  $\text{MoS}_2$ , providing more surface areas and edge sites for methanol adsorption and decomposition into the hydroxide and hydrogen ions [20,50]. The pores of MOFs also adsorb hydroxide ions that can enhance the oxidation of the adsorbed CO and thus regenerate the active sites of catalysts [51]. Consequently, the synergic effect between CoNi-ZIF and  $\text{MoS}_2$  increases hydroxide adsorption and improves catalytic activity and stability. The electron transfer mechanism of  $\text{MoS}_2/\text{CoNi-ZIF}(3-1)$  catalyst surface in alkaline media in MOR possibly obeys the following steps:



### 3.4. HER performances in basic solution

Considering the excellent HER properties of  $\text{MoS}_2$  and good OER activity of CoNi-MOF [52], the HER and OER performances of  $\text{MoS}_2/\text{CoNi-ZIF}$  in alkaline solution was investigated (Figs. 6 and 7). The  $\text{MoS}_2/\text{CoNi-ZIF}$  composite ( $0.14\ \text{mg cm}^{-2}$ ) was directly used as an integrated electrode to catalyze HER under alkaline condition in a three-electrode configuration. Fig. 6a depicts the corrected linear sweep voltammetry (LSV) curves of  $\text{MoS}_2/\text{CoNi-ZIF}$  electrodes obtained at  $10\ \text{mV s}^{-1}$  on the RHE scale in  $1.0\ \text{M KOH}$  solution. For comparison, the LSV curves of  $\text{MoS}_2$ , CoNi-ZIF and commercial Pt/C (20%) catalysts

were obtained under the same condition. As expected, the commercial Pt/C (20%) requires a low overpotential of  $80\ \text{mV}$  at  $10\ \text{mA cm}^{-2}$  ( $\eta_{10}$ ) and an onset potential of  $10\ \text{mV}$  ( $\eta_0$ ). However, the CoNi-ZIF catalyst requires a large overpotential of  $490\ \text{mV}$  to drive HER at a current density of  $10\ \text{mA cm}^{-2}$ , while the overpotential of  $\text{MoS}_2$  is  $420\ \text{mV}$ . Among three kinds of CoNi-ZIF/ $\text{MoS}_2$  composites,  $\text{MoS}_2/\text{CoNi-ZIF}(3-1)$  yields a small  $\eta_0$  of  $50\ \text{mV}$  and  $\eta_{10}$  of  $153\ \text{mV}$ , which are smaller than those of two other composites, namely,  $\text{MoS}_2/\text{CoNi-ZIF}(1-1)$  ( $\eta_0 = 110\ \text{mV}$  and  $\eta_{10} = 220\ \text{mV}$ ) and  $\text{MoS}_2/\text{CoNi-ZIF}(5-1)$  ( $\eta_0 = 90\ \text{mV}$  and  $\eta_{10} = 220\ \text{mV}$ ) (Table S4). This indicates that the electrocatalytic performance of  $\text{MoS}_2/\text{CoNi-ZIF}(3-1)$  toward HER is superior to those of other HER catalysts (Table S5 and Fig. 6b).

The linear portions of Tafel plots of all catalysts were fitted to the Tafel equation ( $\eta = a + b \log j$ ), in which  $j$  is the current density and  $b$  is the Tafel slope (Fig. 6c and Table S4). The results show that  $\text{MoS}_2/\text{CoNi-ZIF}(3-1)$  delivers a Tafel slope of  $68\ \text{mV dec}^{-1}$  that is close to Pt/C ( $65\ \text{mV dec}^{-1}$ ) [53], suggesting that the HER is consistent with the Volmer-Heyrovsky mechanism. The Tafel slopes for  $\text{MoS}_2/\text{CoNi-ZIF}(1-1)$  and  $\text{MoS}_2/\text{CoNi-ZIF}(5-1)$  are also smaller than those of CoNi-ZIF ( $218\ \text{mV dec}^{-1}$ ) and  $\text{MoS}_2$  ( $168\ \text{mV dec}^{-1}$ ). Considering that the Tafel slope is directly associated with the reaction kinetics of electrocatalysts, it is speculated that the lower Tafel slope of  $\text{MoS}_2/\text{CoNi-ZIF}(3-1)$  implies a faster catalytic kinetics and a higher catalytic activity of HER than other materials. Thus, the combination of CoNi-ZIF and  $\text{MoS}_2$  can enhance electrocatalytic activity via a strong synergistic effect between  $\text{MoS}_2$  and CoNi-ZIF.

Durability and stability are vital criteria to assess a catalyst [4]. The stability of  $\text{MoS}_2/\text{CoNi-ZIF}(3-1)$  was first determined by conducting LSV with a potential range of  $-0.4$  to  $-0.1\ \text{V}$  (vs. RHE) at a scan rate of  $100\ \text{mV s}^{-1}$  in  $1.0\ \text{M KOH}$  (Fig. 6d inset). The  $\text{MoS}_2/\text{CoNi-ZIF}(3-1)$  electrode exhibits an increase in the overpotential of  $3\ \text{mV}$  after 5000 LSV cycles to obtain a current density of  $10\ \text{mA cm}^{-2}$ . The HER long-term durability of  $\text{MoS}_2/\text{CoNi-ZIF}(3-1)$  was investigated through electrolysis at a fixed overpotential of  $67\ \text{mV}$ . Consequently, the cathodic current density remains consistent for 48 h of electrolysis (97.5% of the initial value, Fig. 6d), revealing the outstanding stability of  $\text{MoS}_2/\text{CoNi-ZIF}(3-1)$  during HER. However, the cathodic current density of the Pt/C catalyst is only 71.6% of its initial value under the same condition. This is probably attributed to the compositional and structural stability of  $\text{MoS}_2/\text{CoNi-ZIF}(3-1)$ . Further, to understand the effect of Pt wire as a counter electrode on the test results, long-term durability of  $\text{MoS}_2/\text{CoNi-ZIF}(3-1)$  with chronoamperometry test using graphite rod as the counter electrode was measured and the catalyst was characterized by XRD and SEM after stability test. As shown in Fig. S10a, the current density remains 95.2% of the initial value after 48 h. The diffraction peaks of  $\text{MoS}_2$  can be clearly observed (Fig. S10b). Besides, SEM image after 48 h of durability test shows that the  $\text{MoS}_2/\text{CoNi-ZIF}(3-1)$  structure remains similar to the original material (flower-like nanostructure). The results further confirm the excellent stability of  $\text{MoS}_2/\text{CoNi-ZIF}(3-1)$  during electrocatalysis.

The kinetic was tested by EIS at an overpotential of  $150\ \text{mV}$  in  $1.0\ \text{M KOH}$  (Fig. 6e).  $R_{ct}$  is related to the electrocatalytic kinetics at the electrocatalyst/electrolyte interface and a small value corresponds to a fast electron transfer capacity. The EIS spectra display that  $R_{ct}$  for  $\text{MoS}_2/\text{CoNi-ZIF}(3-1)$  is  $42.9\ \Omega$ , which is much smaller than those of  $\text{MoS}_2/\text{CoNi-ZIF}(1-1)$ ,  $\text{MoS}_2/\text{CoNi-ZIF}(5-1)$ , CoNi-ZIF, and  $\text{MoS}_2$  (84, 57.5, 146, and  $168\ \Omega$ , respectively), confirming that  $\text{MoS}_2/\text{CoNi-ZIF}(3-1)$  possesses a fast electron transfer and favorable HER kinetics at the electrocatalyst/electrolyte interface. Compared to the results in  $1.0\ \text{M KOH}$  containing  $0.5\ \text{M CH}_3\text{OH}$  (Fig. S10), the  $R_{ct}$  values for all samples are slightly larger in  $1.0\ \text{M KOH}$  solution, which has been reported in other literature [54]. Electrochemically active surface area (ECSA) of each catalyst was also investigated and compared to enhance the understanding of their HER performance trend and intrinsic activity. Typically, the double-layer capacitance ( $C_{dl}$ ) is linearly proportional to ECSA, which can be investigated by measuring CV curves at different

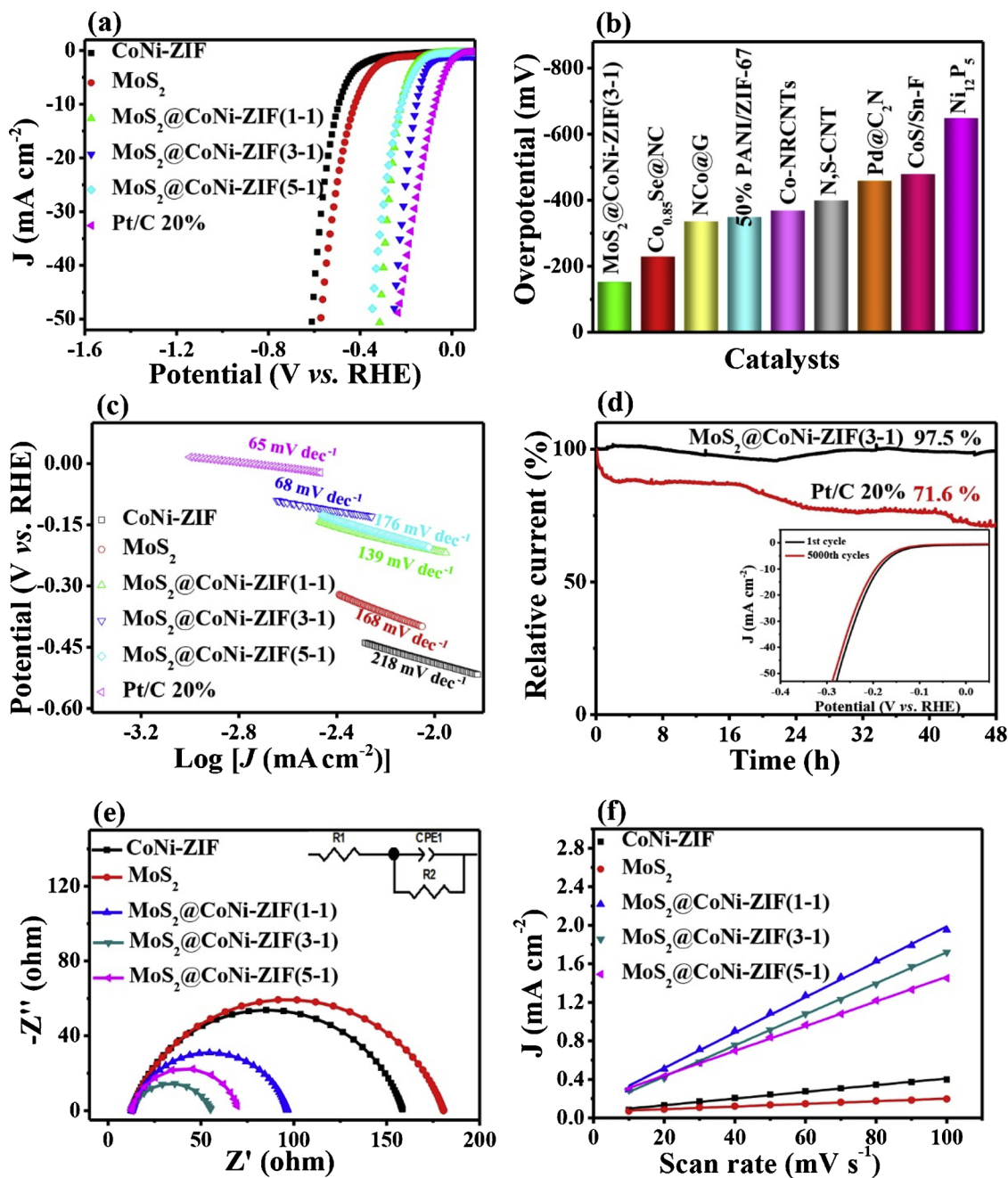


**Fig. 6.** Electrochemical HER measurements. (a) Linear sweep curves in 1.0 M KOH solution of CoNi-ZIF, MoS<sub>2</sub>, MoS<sub>2</sub>@CoNi-ZIF(1-1), MoS<sub>2</sub>@CoNi-ZIF(3-1), MoS<sub>2</sub>@CoNi-ZIF(5-1) and Pt/C (20%). (b) Comparison of the known catalysts of the overpotential at 10 mA cm<sup>-2</sup>. (c) The corresponding Tafel plots of (a). (d) The *I*-*t* responses for MoS<sub>2</sub>@CoNi-ZIF(3-1) and Pt/C at a constant  $\eta_{110}$  of 120 mV (vs. RHE) for 48 h in N<sub>2</sub>-saturated 1.0 M KOH solution (inset: polarization curves of MoS<sub>2</sub>@CoNi-ZIF(3-1) before and after 5000 cycles with scan rate of 10 mV s<sup>-1</sup> between 0.1 and -0.8 V vs. RHE). (e) EIS curves and (f) plots of capacitive currents density ( $j_{\text{anodic}} - j_{\text{cathodic}}$ ) of CoNi-ZIF, MoS<sub>2</sub>, MoS<sub>2</sub>@CoNi-ZIF(1-1), MoS<sub>2</sub>@CoNi-ZIF(3-1), MoS<sub>2</sub>@CoNi-ZIF(5-1) catalysts at 0.15 V vs Ag/AgCl as a function of various scan rates in 1.0 M KOH solution.

scan rates in a nonfaradaic region of 0.1–0.2 V vs. RHE (Fig. S11) [4]. The halves of the differences between positive and negative current densities at the center of the scanning potential ranges are plotted against the scan rates (Fig. 6f) [4]. The calculated  $C_{dl}$  of MoS<sub>2</sub>@CoNi-ZIF(3-1) is 18 mF cm<sup>-2</sup>, which is much higher than those of MoS<sub>2</sub>@CoNi-ZIF(1-1) (16 mF cm<sup>-2</sup>), MoS<sub>2</sub>@CoNi-ZIF(5-1) (12 mF cm<sup>-2</sup>), CoNi-ZIF (3.0 mF cm<sup>-2</sup>), and MoS<sub>2</sub> (1.0 mF cm<sup>-2</sup>). These results confirm that MoS<sub>2</sub>@CoNi-ZIF(3-1) has more effective active sites at the solid-liquid interface, resulting in a higher electrochemical activity for HER.

### 3.5. OER performances in basic solution

Electrocatalytic activities of composites for OER in alkaline solution were also systematically investigated. The homogeneous dispersion of catalyst was dropped on GCE at a constant loading density of 0.14 mg cm<sup>-2</sup> across the samples to maintain a consistent comparison. Electrochemical measurements were taken in 1.0 M O<sub>2</sub>-saturated KOH by using a standard three-electrode system with Ag/AgCl (3.0 M KCl) as a reference electrode and Pt wire as a counter electrode. Fig. 7a shows the corrected LSV curves scanned initially in the anodic direction. All samples exhibit larger current density (*j*). MoS<sub>2</sub>@CoNi-ZIF(1-1) and



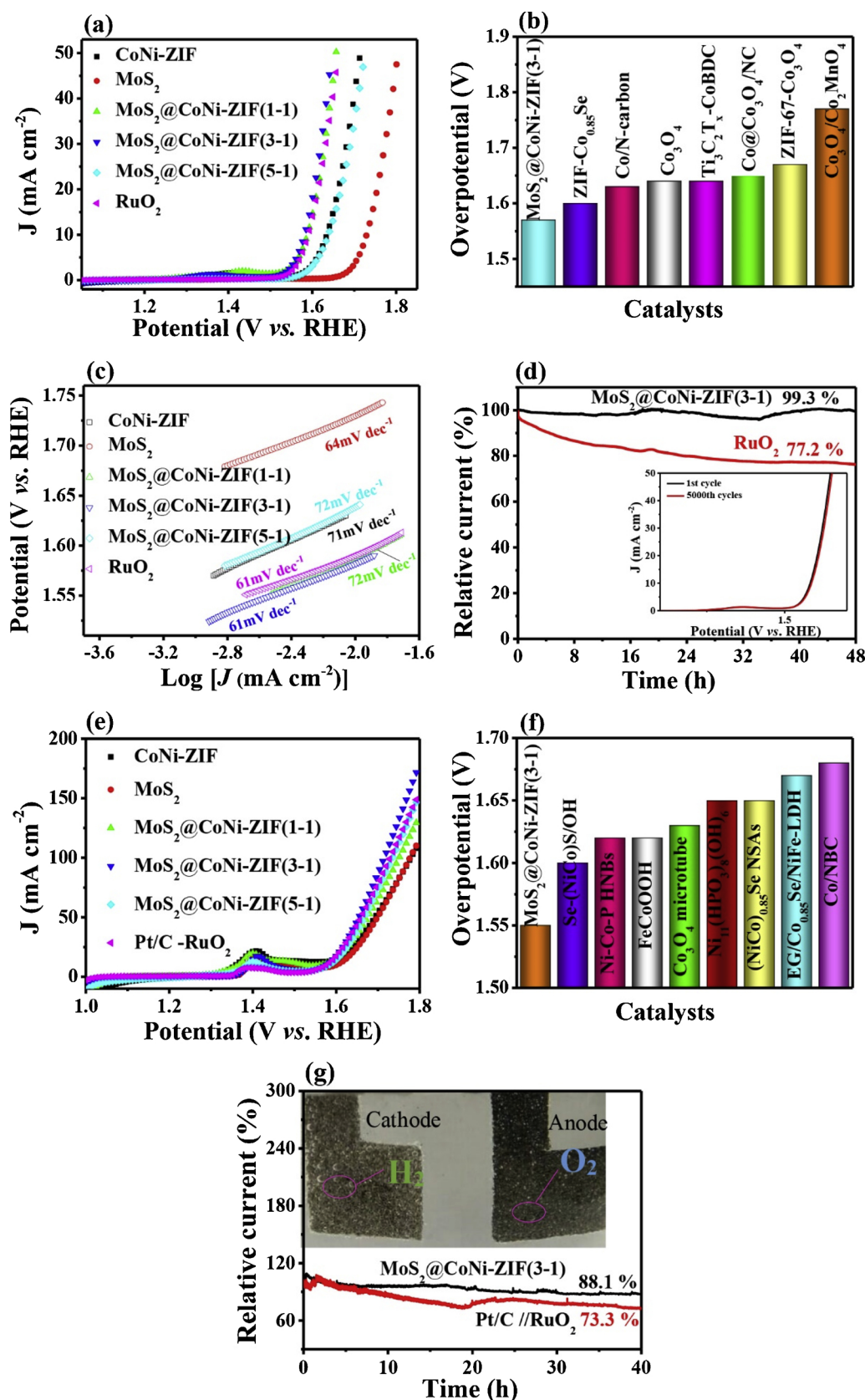


**Fig. 7.** OER performances of catalysts. (a) Polarization curves of CoNi-ZIF, MoS<sub>2</sub>, MoS<sub>2</sub>@CoNi-ZIF(1-1), MoS<sub>2</sub>@CoNi-ZIF(3-1), MoS<sub>2</sub>@CoNi-ZIF(5-1), and RuO<sub>2</sub> (1.0 M KOH, scan rate = 10 mV s<sup>-1</sup>). (b) Comparison with the known catalysts of the overpotential at 10 mA cm<sup>-2</sup>. (c) The corresponding Tafel plots of (a). (d) The  $I$ - $t$  responses for MoS<sub>2</sub>@CoNi-ZIF(3-1) and Pt/C at a constant  $\eta_{10}$  = 1.57 V (vs. RHE) for 48 h in N<sub>2</sub>-saturated 1.0 M KOH solution (inset: polarization curves of MoS<sub>2</sub>@CoNi-ZIF(3-1) before and after 5000 cycles with the scan rate of 10 mV s<sup>-1</sup> between 1.0 and 1.6 V vs. RHE). (e) Polarization curves of CoNi-ZIF, MoS<sub>2</sub>, MoS<sub>2</sub>@CoNi-ZIF(1-1), MoS<sub>2</sub>@CoNi-ZIF(3-1), and MoS<sub>2</sub>@CoNi-ZIF(5-1) composites in the two-electrode electrolyzers at the scan rate of 10 mV s<sup>-1</sup>. (f) Comparison of the reported catalysts of the overpotential at 10 mA cm<sup>-2</sup> in a two electrode electrolyzer. (g) Long-term durability test of MoS<sub>2</sub>@CoNi-ZIF(3-1) electrolyzer at 10 mA cm<sup>-2</sup> and (inset) the photograph during the overall water splitting.

MoS<sub>2</sub>@CoNi-ZIF(3-1) display the earlier onset potential of the catalytic current density, being close to RuO<sub>2</sub>. The overpotential required for achieving a current density of 10 mA cm<sup>-2</sup> should be compared [4]. The MoS<sub>2</sub>@CoNi-ZIF(3-1) catalyst achieves a small  $\eta_{10}$  of only 1.57 V,

which is comparable with that of RuO<sub>2</sub> (1.59 V), showing a superior catalytic ability to those of other tested electrodes (Table S6) and reported catalysts (Fig. 7b). CoNi-ZIF and MoS<sub>2</sub> nanoparticles have the  $\eta_{10}$  of 1.63 and 1.73 V, respectively, giving an inferior catalytic ability.

The Tafel plots derived from the polarization curves of all materials reveal the smallest Tafel slope ( $61 \text{ mV dec}^{-1}$ ) of  $\text{MoS}_2/\text{CoNi-ZIF}(3-1)$  (Fig. 7c and Table S6). Interestingly, although  $\eta_{10}$  of  $\text{MoS}_2$  NSs is large ( $1.73 \text{ V}$ ), a low Tafel slope is obtained ( $64 \text{ mV dec}^{-1}$ ), showing that the OER catalytic kinetics of  $\text{MoS}_2$  is faster than that of  $\text{CoNi-ZIF}$ , which could further improve the OER performance of  $\text{MoS}_2/\text{CoNi-ZIF}$ . In addition, these results reveal that the intrinsic OER catalytic activity of  $\text{MoS}_2/\text{CoNi-ZIF}(3-1)$  is superior to that of  $\text{CoNi-ZIF}$  and  $\text{MoS}_2$ . Also, the OER performance of  $\text{MoS}_2/\text{CoNi-ZIF}(3-1)$  outperforms the  $\text{Co/Ni}$ -based and MOF-derived catalysts (Table S7). The chronopotentiometry curve at a current density of  $10 \text{ mA cm}^{-2}$  for 48 h is obtained to evaluate the durability of  $\text{MoS}_2/\text{CoNi-ZIF}(3-1)$ . In Fig. 7d, no significant increase in the overpotential is found during continuous electrolysis for 48 h, showing good stability of  $\text{MoS}_2/\text{CoNi-ZIF}(3-1)$ . The overpotential is only 77.2% of the initial value at the same conditions for  $\text{RuO}_2$ . The stability of  $\text{MoS}_2/\text{CoNi-ZIF}(3-1)$  was also evaluated by continuous sweeps of LSV (scan rate  $10 \text{ mV s}^{-1}$ ,  $1.0 \text{ M KOH}$  solution) (Fig. 7d inset), and the polarization curve shows a limited decay after 5000 cycles. The outstanding OER activity and good stability of  $\text{MoS}_2/\text{CoNi-ZIF}(3-1)$  reveal its potential applications.

### 3.6. Water splitting performances of $\text{MoS}_2/\text{CoNi-ZIF}(3-1)$

A two-electrode electrolyzer was assembled and tested for the overall water splitting, in terms of its good bifunctional characteristics of  $\text{MoS}_2/\text{CoNi-ZIF}(3-1)$  in both HER and OER (Tables S5 and S7). As shown in Fig. 7e, it shows that only  $1.55 \text{ V}$  cell potential is required to attain a current density of  $10 \text{ mA cm}^{-2}$  for  $\text{MoS}_2/\text{CoNi-ZIF}(3-1)$ , which is comparable to that of commercial  $\text{Pt/C}/\text{RuO}_2$  couple ( $1.57 \text{ V}$ ). Also, the catalytic ability of  $\text{MoS}_2/\text{CoNi-ZIF}(3-1)$  for the overall water splitting is superior to those of  $\text{MoS}_2/\text{CoNi-ZIF}(1-1)$  ( $1.58 \text{ V}$ ) and  $\text{MoS}_2/\text{CoNi-ZIF}(5-1)$  ( $1.57 \text{ V}$ ). These results show that  $\text{MoS}_2/\text{CoNi-ZIF}(3-1)$  is one of leading electrocatalysts compared with the known noble metal free bifunctional catalysts such as  $\text{EG/Co}_{0.85}\text{Se/NiFe-LDH}$  ( $1.67 \text{ V}$ ),  $\text{Ni-Co-P HNBs}$  ( $1.62 \text{ V}$ ),  $\text{Ni}_{11}(\text{HPO}_3)_8(\text{OH})_6$  ( $1.65 \text{ V}$ ),  $\text{Ni-Co}_{0.85}\text{Se NSAs}$  ( $1.65 \text{ V}$ ), and  $\text{Se-(NiCo)S/OH}$  ( $1.60 \text{ V}$ ) (Table S8 and Fig. 7f). The initial activity of  $\text{MoS}_2/\text{CoNi-ZIF}(3-1)$  after 40 h is remarkably retained (88.1%) compared with that of the commercial  $\text{Pt/C}/\text{RuO}_2$  couple (73.3% of the initial value). Fig. 7g inset clearly shows gas bubbles produced both on anode and cathode, revealing a great potential of  $\text{MoS}_2/\text{CoNi-ZIF}(3-1)$  towards overall water splitting in alkaline solution. The excellent catalytic performances of  $\text{MoS}_2/\text{CoNi-ZIF}$  in HER and OER could be attributed to the following reasons: (i) a vertical growth of  $\text{MoS}_2$  NSs on  $\text{CoNi-ZIF}$  surface can enhance the HER capacity via exposing more active edge sites [55]; (ii) the integration of  $\text{Co/Ni}$  and  $\text{MoS}_2$  NSs would change the electronic structure of catalyst, thus improving the intrinsic conductivity [56]; (iii) the presence of metallic states  $\text{Co}$  and  $\text{Ni}$  leads to a strong affinity to hydride intermediate during HER for its metallic properties [52] and could serve as the dominating active centers for OER [57]; (iv) the synergistic effect between  $\text{CoNi-ZIF}$  and  $\text{MoS}_2$  NSs plays a key role in improving the catalytic performance for HER or OER; (v) the  $\text{CoNi-ZIF}$  template efficiently prevents  $\text{MoS}_2$  NSs from assembling, resulting in the unique heterostructure of  $\text{MoS}_2/\text{CoNi-ZIF}(3-1)$ .

### 3.7. Post-catalytic structural analyses of $\text{MoS}_2/\text{CoNi-ZIF}(3-1)$

$\text{MoS}_2/\text{CoNi-ZIF}(3-1)$  used for 48 h of overall water splitting was studied by XPS, XRD, and SEM. The chemical compositions in the XPS survey spectrum do not substantially change after the durability tests were completed (Fig. S12a). The high-resolution XPS spectrum of  $\text{Co } 2p$  illustrates that the peak intensity of  $\text{Co}^0$  species increases (Fig. S12b), suggesting that a part of  $\text{Co}^{2+}$  in  $\text{MoS}_2/\text{CoNi-ZIF}(3-1)$  was reduced to  $\text{Co}^0$  species, which is consistent with previous reports [58]. The XPS spectra of  $\text{Ni}$ ,  $\text{Mo}$ , and  $\text{S}$  elements do not obviously change compared with the original results (Figs. S12c–e), indicating that  $\text{Ni}$ ,  $\text{Mo}$ , and  $\text{S}$

have the same valence states after the durability tests. These results suggest that  $\text{MoS}_2/\text{CoNi-ZIF}(3-1)$  is stable in harsh alkaline environment. The XRD pattern (Fig. S12f) and SEM (Fig. S12g) image of the  $\text{MoS}_2/\text{CoNi-ZIF}(3-1)$  after 48 h of durability test reveal that the composition and NS structure remain similar to that of the original material. These results imply the good stability of  $\text{MoS}_2/\text{CoNi-ZIF}(3-1)$  during the overall water splitting reaction.

## 4. Conclusion

In summary, we propose an earth-abundant element electrocatalyst for highly efficient methanol electro-oxidation and overall water splitting, which is achieved by the entrapment of  $\text{MoS}_2$  layer around a hollow  $\text{CoNi-ZIF}$  nanostructure. Among the series of  $\text{MoS}_2/\text{CoNi-ZIF}$  composites, a considerable enhancement in oxidation peak current density is observed in the electrode based on  $\text{MoS}_2/\text{CoNi-ZIF}(3-1)$ , thereby exhibiting a superior electrocatalytic activity in MOR. Concurrently, it gives a cell voltage of only  $1.55 \text{ V}$  at the potential of  $10 \text{ mV cm}^{-2}$  during the overall water splitting in a two-electrode electrolysis cell in alkaline solution. As compared with other catalysts, the proposed  $\text{MoS}_2/\text{CoNi-ZIF}(3-1)$  catalyst has three substantial advantages, (i) multiple catalytic performances for MOR and water splitting in alkaline solution, (ii) feasible synthesis without requiring calcination or other treatments, and (iii) strong synergistic effect among  $\text{CoNi-ZIF}$ , metal oxide and  $\text{MoS}_2$ , providing  $\text{MoS}_2/\text{CoNi-ZIF}$  with both excellent performance and high stability. This work provides a basis for developing new multifunctional catalysts for high-efficiency DMFCs and high-performance clean energy.

## Declaration of Competing Interest

The authors declare that they have no known competing financial interests or personal relationships that could have appeared to influence the work reported in this paper.

## Acknowledgements

We are grateful to the financial support from the National Natural Science Foundation of China (21571158 & 21601161), Program for Science & Technology Innovation Talents in Universities of Henan Province (19HASTIT050), Innovative Technology Team of Henan Province (CXTD2014042), and the Key Research Project of University of Henan Province (19zx004).

## Appendix A. Supplementary data

Supplementary material related to this article can be found, in the online version, at doi:<https://doi.org/10.1016/j.apcatb.2019.117970>.

## References

- [1] N. Naresh, P. Karthik, R. Vinodh, C. Muthamizhchelvan, B. Neppolian, Tailoring multi-metallic nanotubes by copper nanowires with platinum and gold via galvanic replacement route for the efficient methanol oxidation reaction, *Electrochim. Acta* 282 (2018) 792–798.
- [2] G. Zhao, K. Rui, S.X. Dou, W. Sun, Heterostructures for electrochemical hydrogen evolution reaction: a review, *Adv. Funct. Mater.* 28 (2018) 1803291.
- [3] L. He, J. Liu, Y. Liu, B. Cui, B. Hu, M. Wang, K. Tian, Y. Song, S. Wu, Z. Zhang, Z. Peng, M. Du, Titanium dioxide encapsulated carbon-nitride nanosheets derived from MXene and melamine-cyanuric acid composite as a multifunctional electrocatalyst for hydrogen and oxygen evolution reaction and oxygen reduction reaction, *Appl. Catal. B: Environ.* 248 (2019) 366–379.
- [4] B. Cui, B. Hu, J. Liu, M. Wang, Y. Song, K. Tian, Z. Zhang, L. He, Solution-plasma-assisted bimetallic oxide alloy nanoparticles of Pt and Pd embedded within two-dimensional  $\text{Ti}_3\text{C}_2\text{T}_x$  nanosheets as highly active electrocatalysts for overall water splitting, *ACS Appl. Mater. Interface* 10 (2018) 23858–23873.
- [5] G.M. Tomboc, M.W. Abebe, A.F. Baye, H. Kim, Utilization of the superior properties of highly mesoporous PVP modified  $\text{NiCo}_2\text{O}_4$  with accessible 3D nanostructure and flower-like morphology towards electrochemical methanol oxidation reaction, *J. Energy Chem.* 29 (2019) 136–146.
- [6] X. Cui, P. Xiao, J. Wang, M. Zhou, W. Guo, Y. Yang, Y. He, Z. Wang, Y. Yang,

- Y. Zhang, Z. Lin, Highly branched metal alloy networks with superior activities for the methanol oxidation reaction, *Angew. Chem. Int. Ed.* 56 (2017) 4488–4493.
- [7] B. Dong, W. Li, X. Huang, Z. Ali, T. Zhang, Z. Yang, Y. Hou, Fabrication of hierarchical hollow Mn doped Ni(OH)<sub>2</sub> nanostructures with enhanced catalytic activity towards electrochemical oxidation of methanol, *Nano Energy* 55 (2019) 37–41.
- [8] J. Wang, F. Xu, H. Jin, Y. Chen, Y. Wang, Non-noble metal-based carbon composites in hydrogen evolution reaction: fundamentals to applications, *Adv. Mater.* 29 (2017) 1605838.
- [9] B. Zhao, M.M. Collinson, Well-defined hierarchical templates for multimodal porous material fabrication, *Chem. Mater.* 22 (2010) 4312–4319.
- [10] Y. Song, F. Duan, S. Zhang, J. Tian, Z. Zhang, Z. Wang, C. Liu, W. Xu, M. Du, Iron oxide@mesoporous carbon architectures derived from an Fe(II)-based metal-organic framework for highly sensitive oxytetracycline determination, *J. Mater. Chem. A* 5 (2017) 19378–19389.
- [11] A. Banerjee, U. Singh, V. Aravindan, M. Srinivasan, S. Ogale, Synthesis of CuO nanostructures from Cu-based metal organic framework (MOF-199) for application as anode for Li-ion batteries, *Nano Energy* 2 (2013) 1158–1163.
- [12] M. Wang, L. Yang, C. Guo, X. Liu, L. He, Y. Song, Q. Zhang, X. Qu, H. Zhang, Z. Zhang, S. Fang, Bimetallic Fe/Ti-based metal–organic framework for persulfate-assisted visible light photocatalytic degradation of orange II, *ChemistrySelect* 3 (2018) 3664–3674.
- [13] N. Cheng, L. Ren, X. Xu, Y. Du, S.X. Dou, Recent development of zeolitic imidazolate frameworks (ZIFs) derived porous carbon-based materials as electrocatalysts, *Adv. Energy Mater.* 8 (2018) 1801257.
- [14] T. Wang, Z. Kou, S. Mu, J. Liu, D. He, I.S. Amiin, W. Meng, K. Zhou, Z. Luo, S. Chaemchuen, F. Verpoort, 2D dual-metal zeolitic-imidazolate-framework-(ZIF)-derived bifunctional air electrodes with ultrahigh electrochemical properties for rechargeable zinc-air batteries, *Adv. Funct. Mater.* 28 (2018) 1705048.
- [15] X. Xiao, C. He, S. Zhao, J. Li, W. Lin, Z. Yuan, Q. Zhang, S. Wang, L. Dai, D. Yu, A general approach to cobalt-based homobimetallic phosphide ultrathin nanosheets for highly efficient oxygen evolution in alkaline media, *Energy Environ. Sci.* 10 (2017) 893–899.
- [16] Y. Wen, Z. Wei, C. Ma, X. Xing, Z. Li, D. Luo, MXene boosted CoNi-ZIF-67 as highly efficient electrocatalysts for oxygen evolution, *Nanomaterials* 9 (2019) 775.
- [17] D. Lyu, Y.B. Mollamahale, S. Huang, P. Zhu, X. Zhang, Y. Du, S. Wang, M. Qing, Z.Q. Tian, P.K. Shen, Ultra-high surface area graphitic Fe-N-C nanospheres with single-atom iron sites as highly efficient non-precious metal bifunctional catalysts towards oxygen redox reactions, *J. Catal.* 368 (2018) 279–290.
- [18] H. Li, F. Ke, J. Zhu, MOF-derived ultrathin cobalt phosphide nanosheets as efficient bifunctional hydrogen evolution reaction and oxygen evolution reaction electrocatalysts, *Nanomaterials* 8 (2018) 89.
- [19] T. Huang, Y. Chen, J. Lee, Two-dimensional cobalt/N-doped carbon hybrid structure derived from metal–organic frameworks as efficient electrocatalysts for hydrogen evolution, *ACS Sustain. Chem. Eng.* 5 (2017) 5646–5650.
- [20] R. Mehek, N. Iqbal, T. Noor, H. Nasir, Y. Mehmood, S. Ahmed, Novel Co-MOF/graphene oxide electrocatalyst for methanol oxidation, *Electrochim. Acta* 255 (2017) 195–204.
- [21] X. Wu, J. Zhao, Y. Wu, W. Dong, D. Li, J. Li, Q. Zhang, Ultrafine Pt nanoparticles and amorphous nickel supported on 3D mesoporous carbon derived from Cu-metal–organic framework for efficient methanol oxidation and nitrophenol reduction, *ACS Appl. Mater. Interface* 10 (2018) 12740–12749.
- [22] D. Zhu, L. Li, J. Cai, M. Jiang, J. Qi, X. Zhao, Nitrogen-doped porous carbons from bipyridine-based metal–organic frameworks: electrocatalysis for oxygen reduction reaction and Pt-catalyst support for methanol electrooxidation, *Carbon* 79 (2014) 544–553.
- [23] Y. Li, K. Yin, L. Wang, X. Lu, Y. Zhang, Y. Liu, D. Yan, Y. Song, S. Luo, Engineering MoS<sub>2</sub> nanomesh with holes and lattice defects for highly active hydrogen evolution reaction, *Appl. Catal. B: Environ.* 239 (2018) 537–544.
- [24] Y. Li, L. Wang, T. Cai, S. Zhang, Y. Liu, Y. Song, X. Dong, L. Hu, Glucose-assisted synthesis 1D/2D nearly vertical CdS/MoS<sub>2</sub> heterostructures for efficient photocatalytic hydrogen evolution, *Chem. Eng. J.* 321 (2017) 366–374.
- [25] Y. Liu, X. Zhou, T. Ding, C. Wang, Q. Yang, 3D architecture constructed via the confined growth of MoS<sub>2</sub> nanosheets in nanoporous carbon derived from metal–organic frameworks for efficient hydrogen production, *Nanoscale* 7 (2015) 18004–18009.
- [26] X. Su, J. Ning, Y. Jia, Y. Liu, Flower-like MoS<sub>2</sub> nanospheres: a promising material with good microwave absorption property in the frequency range of 8.2–12.4 GHz, *Nano* 13 (2018) 1850084.
- [27] B. Wang, Y. Zhang, J. Zhang, R. Xia, Y. Chu, J. Zhou, X. Yang, J. Huang, Facile synthesis of a MoS<sub>2</sub> and functionalized graphene heterostructure for enhanced lithium-storage performance, *ACS Appl. Mater. Interface* 9 (2017) 12907–12913.
- [28] J. Zhu, X. Zhao, M. Xiao, L. Liang, C. Liu, J. Liao, W. Xing, The construction of nitrogen-doped graphitized carbon-TiO<sub>2</sub> composite to improve the electrocatalyst for methanol oxidation, *Carbon* 72 (2014) 114–124.
- [29] M.W. Louie, A.T. Bell, An investigation of thin-film Ni-Fe oxide catalysts for the electrochemical evolution of oxygen, *J. Am. Chem. Soc.* 135 (2013) 12329–12337.
- [30] O. Guellati, A. Harat, D. Momodu, J. Dangbegnon, T. Romero, D. Begin, C. Pham-Huu, N. Manyala, M. Guerroune, Electrochemical measurements of 1D/2D/3D Ni-Co bi-phase mesoporous nanohybrids synthesized using free-template hydrothermal method, *Electrochim. Acta* 275 (2018) 155–171.
- [31] Y. Zhou, Z. Zhou, R. Shen, R. Ma, Q. Liu, G. Cao, J. Wang, Correlating electrocatalytic oxygen reduction activity with d-band centers of metallic nanoparticles, *Energy Storage Mater.* 13 (2018) 189–198.
- [32] H. Sun, Y. Lian, C. Yang, L. Xiong, P. Qi, Q. Mu, X. Zhao, J. Guo, Z. Deng, Y. Peng, A hierarchical nickel-carbon structure templated by metal–organic frameworks for efficient overall water splitting, *Energy Environ. Sci.* 11 (2018) 2363–2371.
- [33] Z. Peng, D. Jia, A.M. Al-Enizi, A.A. Elzathary, G. Zheng, From water oxidation to reduction: homologous Ni-Co based nanowires as complementary water splitting electrocatalysts, *Adv. Energy Mater.* 5 (2015) 1402031.
- [34] Z. Liang, C. Qu, D. Xia, R. Zou, Q. Xu, Atomically dispersed metal sites in MOF-based materials for electrocatalytic and photocatalytic energy conversion, *Angew. Chem. Int. Ed.* 57 (2018) 9604–9633.
- [35] H. Zhou, R. Zhang, S. Song, C. Xiao, G. Gao, S. Ding, Dopamine-assisted synthesis of MoS<sub>2</sub> nanosheets on carbon nanotube for improved lithium and sodium storage properties, *ACS Appl. Energy Mater.* 1 (2018) 5112–5118.
- [36] Z. Gao, N. Song, X. Li, Microstructural design of hybrid CoO@NiO and graphene nano-architectures for flexible high-performance supercapacitors, *J. Mater. Chem. A* 3 (2015) 14833–14844.
- [37] L. He, B. Cui, J. Liu, M. Wang, Z. Zhang, H. Zhang, Fabrication of porous CoO<sub>x</sub>/mC@MoS<sub>2</sub> composite loaded on g-C<sub>3</sub>N<sub>4</sub> nanosheets as a highly efficient dual electrocatalyst for oxygen reduction and hydrogen evolution reactions, *ACS Sustain. Chem. Eng.* 6 (2018) 9257–9268.
- [38] H. Yuan, Y. Hou, I.M. Abu-Reesh, J. Chen, Z. He, Oxygen reduction reaction catalysts used in microbial fuel cells for energy-efficient wastewater treatment: a review, *Mater. Horiz.* 3 (2016) 382–401.
- [39] A.K. Das, R.K. Layek, N.H. Kim, D. Jung, J.H. Lee, Reduced graphene oxide (RGO)-supported NiCo<sub>2</sub>O<sub>4</sub> nanoparticles: an electrocatalyst for methanol oxidation, *Nanoscale* 6 (2014) 10657–10665.
- [40] N.V. Kosova, E.T. Devyatkina, V.V. Kaichev, Optimization of Ni<sup>2+</sup>/Ni<sup>3+</sup> ratio in layered Li(Ni,Mn,Co)O<sub>2</sub> cathodes for better electrochemistry, *J. Power Sources* 174 (2007) 965–969.
- [41] Y. Sun, Y. Zhou, C. Zhu, W. Tu, H. Wang, H. Huang, Y. Liu, M. Shao, J. Zhong, S. Lee, Z. Kang, Synergistic Cu@CoO<sub>x</sub> core-shell structure on carbon layers as highly active and durable electrocatalysts for catechol oxidation, *Appl. Catal. B: Environ.* 244 (2019) 795–801.
- [42] Y. Wang, Z. Chen, T. Lei, Y. Ai, Z. Peng, X. Yan, H. Li, J. Zhang, Z.M. Wang, Y. Chueh, Hollow NiCo<sub>2</sub>S<sub>4</sub> nanospheres hybridized with 3D hierarchical porous rGO/Fe<sub>2</sub>O<sub>3</sub> composites toward high-performance energy storage device, *Adv. Energy Mater.* 8 (2018) 1703453.
- [43] H. Sun, Y. Ye, J. Liu, Z. Tian, Y. Cai, P. Li, C. Liang, Pure Ni nanocrystallines anchored on rGO present ultrahigh electrocatalytic activity and stability in methanol oxidation, *Chem. Commun.* 54 (2018) 1563–1566.
- [44] A.A. Gewirth, J.A. Varnell, A.M. DiAscro, Nonprecious metal catalysts for oxygen reduction in heterogeneous aqueous systems, *Chem. Rev.* 118 (2018) 2313–2339.
- [45] N. Zhou, L. Yang, B. Hu, Y. Song, L. He, W. Chen, Z. Zhang, Z. Liu, S. Lu, Core-shell heterostructured CuFe@FeFe prussian blue analogue coupling with silver nanoclusters via a one-step bioinspired approach: efficiently nonlabeled aptasensor for detection of bleomycin in various aqueous environments, *Anal. Chem.* 90 (2018) 13624–13631.
- [46] Z. Xue, P. Wang, A. Peng, T. Wang, Architectural design of self-assembled hollow superstructures, *Adv. Mater.* (2018) 1801441.
- [47] B. Wang, Y. Cao, Y. Chen, R. Wang, X. Wang, X. Lai, C. Xiao, J. Tu, S. Ding, Microwave-assisted fast synthesis of hierarchical NiCo<sub>2</sub>O<sub>4</sub> nanoflower-like supported Ni(OH)<sub>2</sub> nanoparticles with an enhanced electrocatalytic activity towards methanol oxidation, *Inorg. Chem. Front.* 5 (2018) 172–182.
- [48] A.R. Jadhav, H.A. Bandal, A.A. Chaugule, H. Kim, Diethylenetriamine assisted synthesis of mesoporous Co and Ni-Co spinel oxides as an electrocatalysts for methanol and water oxidation, *Electrochim. Acta* 240 (2017) 277–287.
- [49] L. Gong, Z. Yang, K. Li, J. Ge, C. Liu, X. Wei, Recent development of methanol electrooxidation catalysts for direct methanol fuel cell, *J. Energy Chem.* 27 (2018) 1618–1628.
- [50] A. Muthurasu, V. Maruthapandian, H.Y. Kim, Metal–organic framework derived Co<sub>3</sub>O<sub>4</sub>/MoS<sub>2</sub> heterostructure for efficient bifunctional electrocatalysts for oxygen evolution reaction and hydrogen evolution reaction, *Appl. Catal. B: Environ.* 248 (2019) 202–210.
- [51] K. Otake, Y. Cui, C.T. Buru, Z. Li, J.T. Hupp, O.K. Farha, Single-atom-based vanadium oxide catalysts supported on metal–organic frameworks: selective alcohol oxidation and structure-activity relationship, *J. Am. Chem. Soc.* 140 (2018) 8652–8656.
- [52] M. Liu, W. Zheng, S. Ran, S.T. Boles, L.Y.S. Lee, Overall water-splitting electrocatalysts based on 2D CoNi-metal–organic frameworks and its derivative, *Adv. Mater. Interface* 5 (2018) 1800849.
- [53] J. Deng, P. Ren, D. Deng, L. Yu, F. Yang, X. Bao, Highly active and durable non-precious-metal catalysts encapsulated in carbon nanotubes for hydrogen evolution reaction, *Energy Environ. Sci.* 7 (2014) 1919–1923.
- [54] I.S. Pieta, A. Rathi, P. Pieta, R. Nowakowski, M. Hójdynski, M. Pisarek, A. Kaminska, M.B. Gawande, R. Zboril, Electrocatalytic methanol oxidation over Cu, Ni and bimetallic Cu-Ni nanoparticles supported on graphitic carbon nitride, *Appl. Catal. B: Environ.* 244 (2019) 272–283.
- [55] T.F. Jaramillo, K.P. Jørgensen, J. Bonde, J.H. Nielsen, S. Hørch, I. Chorkendorff, Identification of active edge sites for electrochemical H<sub>2</sub> evolution from MoS<sub>2</sub> nanocatalysts, *Science* 317 (2007) 100–102.
- [56] J. Deng, H. Li, S. Wang, D. Ding, M. Chen, C. Liu, Z. Tian, K.S. Novoselov, C. Ma, D. Deng, X. Bao, Multiscale structural and electronic control of molybdenum disulfide foam for highly efficient hydrogen production, *Nat. Commun.* 8 (2017) 14430.
- [57] S. Zhao, Y. Wang, J. Dong, C. He, H. Yin, P. An, K. Zhao, X. Zhang, C. Gao, L. Zhang, J. Lv, J. Wang, J. Zhang, A.M. Khatkhat, N.A. Khan, Z. Wei, J. Zhang, S. Liu, H. Zhao, Z. Tang, Ultrathin metal–organic framework nanosheets for electrocatalytic oxygen evolution, *Nat. Energy* 1 (2016) 16184.
- [58] L. He, B. Cui, B. Hu, J. Liu, K. Tian, M. Wang, Y. Song, S. Fang, Z. Zhang, Q. Jia, Mesoporous nanostructured CoFe-Se-P composite derived from a prussian blue analogue as a superior electrocatalyst for efficient overall water splitting, *ACS Appl. Energy Mater.* 1 (2018) 3915–3928.